JOURNAL OF GEOPHYSICAL RESEARCH: SPACE PHYSICS, VOL. 118, 1571–1588, doi:10.1002/jgra.50234, 2013

Current structure and nonideal behavior at magnetic null points in the turbulent magnetosheath

D. E. Wendel[1] and M. L. Adrian[1]

Received 15 October 2012; revised 27 February 2013; accepted 10 March 2013; published 25 April 2013.

[1] The Poincaré index indicates that the Cluster spacecraft tetrahedron entraps a number of 3-D magnetic nulls during an encounter with the turbulent magnetosheath. Previous researchers have found evidence for reconnection at one of the many filamentary current layers observed by Cluster in this region. We find that many of the entrained nulls are also associated with strong currents. We dissect the current structure of a pair of spiral nulls that may be topologically connected. At both nulls, we find a strong current along the spine, accompanied by a somewhat more modest current perpendicular to the spine that tilts the fan toward the axis of the spine. The current along the fan is comparable to the that along the spine. At least one of the nulls manifests a rotational flow pattern in the fan plane that is consistent with torsional spine reconnection as predicted by theory. These results emphasize the importance of examining the magnetic topology in interpreting the nature of currents and reconnection in 3-D turbulence.

Citation: Wendel, D. E., and M. L. Adrian (2013), Current structure and nonideal behavior at magnetic null points in the turbulent magnetosheath, *J. Geophys. Res. Space Physics*, *118*, 1571–1588, doi:10.1002/jgra.50234.

1. Introduction

[2] Recent observations have explored the nature of current sheets in turbulence [*Eastwood et al.*, 2009; *Lazarian et al.*, 2009; *Matthaeus et al.*, 2003; *Osman and Horbury*, 2009; *Osman et al.*, 2011; *Retinò et al.*, 2007]. The current sheets within the turbulence are usually affiliated with some kind of magnetic reconnection that leads to plasma heating and thus offer one explanation to the problem of non-adiabatic heating of the solar wind [*Boldyrev*, 2006; *Coleman*, 1968; *Cranmer et al.*, 2009; *Goldstein et al.*, 1995; *Lazarian et al.*, 2009; *Matthaeus et al.*, 1994; *Vasquez et al.*, 2007; *Verma et al.*, 1995; *Zank et al.*, 1996]. In turn, simulations have shown that turbulence can augment the reconnection rate [*Matthaeus and Lamkin*, 1985, 1986; *Servidio et al.*, 2009; *Servidio et al.*, 2010], and observations have likewise associated turbulence with fast reconnection [*Ji et al.*, 2004; *Retinò et al.*, 2007; *Sundkvist et al.*, 2007], thus providing one explanation of the problem of fast reconnection in high-Lundquist-number systems such as the Sun's corona and the Earth's magnetosphere. Moreover, theory, observations, and simulations have demonstrated the 3-D nature of reconnection at the Sun and the Earth [*Che et al.*, 2011; *Daughton et al.*, 2011; *Deng et al.*, 2009; *Parnell et al.*, 2008; *Pontin et al.*, 2005b; *Priest and Titov*, 1996]. In fact, 3-D reconnection engenders turbulence in high-resolution kinetic simulations [*Che et al.*, 2011; *Daughton et al.*, 2011]. While researchers have observed 3-D turbulent reconnection in the laboratory and in simulations, and others have discovered in situ spacecraft observations of 3-D reconnection [*Deng et al.*, 2009; *He et al.*, 2008; *Xiao et al.*, 2006], in situ observations of *turbulent* reconnection have yet to be analyzed from a 3-D perspective. To this date, analyses of spacecraft observations have treated turbulent reconnecting current sheets from a 2-D point of view [*Eastwood et al.*, 2009; *Greco et al.*, 2010; *Greco et al.*, 2009; *Retinò et al.*, 2007; *Sundkvist et al.*, 2007]. While this may be appropriate in regions with a guide field, it is in general not sufficient. In this work, we apply topological measures to in situ spacecraft observations of turbulent filamentary currents to uncover their 3-D nature.

1.1. Turbulent Reconnection

[3] The role of turbulence in 2-D magnetic reconnection first acquired attention in the 1980s. In their 2-D MHD simulations, *Matthaeus and Lamkin* [1985] and *Matthaeus and Lamkin* [1986] found turbulence enabled fast reconnection, and others [*Bhattacharjee et al.*, 2009; *Smith et al.*, 2004] have derived 2-D scaling laws for the contribution of secondary islands and turbulence to the reconnection rate. In recent statistical surveys of 2.5-D MHD turbulence, *Servidio et al.* [2009] find reconnecting current sheets with a range of reconnection rates associated with a range of magnetic island sizes. In a statistical analysis of dissipation measures in a 2-D particle-in-cell (PIC) simulation of turbulent reconnection, *Wan et al.* [2012] discover coherent structures on ion to electron scales and a correlation between the strongest current sheets and the largest dissipation rates.

[4] Theoretical analyses and recent 3-D PIC simulations of reconnection with a guide field reveal a relationship between the three dimensions and the development of turbulence and ensuing fast reconnection [*Che et al.*, 2011; *Daughton et al.*, 2011]. In simulations with 3-D dependence, turbulence is not assumed, as in the 2-D simulations, but,

[1]NASA Goddard Space Flight Center, Greenbelt, Maryland, USA.

Corresponding author: D. E. Wendel, NASA Goddard Space Flight Center, Greenbelt, MD, USA. (deirdre.e.wendel@nasa.gov)

2169-9380/13/10.1002/jgra.50234

rather, is a consequence of reconnection. Nevertheless, as in the 2-D simulations, layers of interacting magnetic islands and vortices that are limned by thin, filamentary current layers characterize the turbulence. *Strauss* [1988] derived fast reconnection rates from a theoretical analysis of low-β, 3-D, MHD tearing mode turbulence.

[5] Space observations of turbulence and embedded, reconnecting current layers include observations of the Sun, the solar wind, and the Earth's magnetosphere. Solar observations have found reconnection within a framework of 3-D topology and fragmented, stochastic fields [*Albright*, 1999; *Parnell*, 2007; *Schrijver and Title*, 2002]. Studies of turbulence in the solar wind [*Matthaeus et al*., 2003; *Osman and Horbury*, 2009; *Osman et al*., 2011; *Sahraoui et al*., 2009; *Sahraoui et al*., 2010] attribute heating to small-scale reconnecting current sheets. Several geospace observations in the magnetotail [*Eastwood et al*., 2009] and in the magnetosheath [*Retinò et al*., 2007; *Sundkvist et al*., 2007] have analyzed reconnection in turbulence. These observers, however, have analyzed the current sheets as 2-D structures, which may be of limited validity.

1.2. 3-D Reconnection

[6] The 3-D magnetic topological skeleton consists of magnetic nulls, spines, separators, and separatrices. In strong background fields, quasi-separatrix layers can take the place of separatrices and null points. Magnetic null points are produced in pairs of opposite polarity. A spine and a fan—or separatrix surface—define a magnetic null point. The spine, γ, consists of a field line that emanates either toward or away from a null on opposite sides of the null, and the fan planes, Σ, comprise the surface of field lines that spread away from or toward the null (see Figure 1a). The polarity of a null in three dimensions is positive if the spine points toward the null and negative if it points away from the null. A type A (type B) null is a negative (positive) null with radial fan field lines, while a type A_S (type B_S) null is a negative (positive) null with spiraling fan field lines [*Lau and Finn*, 1990; *Parnell et al*., 1996] (Figure 1b). Generally, the fan field lines in type A and type B nulls align themselves more or less along one fan axis to form what is called an improper radial null [*Parnell et al*., 1996]. Magnetic null points may be potential (current-free) or nonpotential (currents in the spine, or fan, or both) [*Parnell et al*., 1996]. The spines and fans of magnetic nulls and the loci where the fans of pairs of nulls intersect—i.e., the separator—define the magnetic topology around the null point (see Figure 1c). A quasi-separatrix layer is a layer of field lines oriented perpendicular to an *x*-type magnetic geometry, but where a strong guide field may still be present [*Priest and Forbes*, 2000].

[7] Researchers have shown that reconnection is feasible on various elements of the magnetic topology. For example, where topological separators exist, 3-D reconnection often occurs on the magnetic separator [*Dorelli et al*., 2007; *Parnell et al*., 2008; *Priest and Forbes*, 2000]. The separator may be global (such as across the Earth's dayside magnetopause) or local (as in the smaller scales of a turbulent system or tearing mode) [*Priest and Forbes*, 2000]. *Priest and Forbes* [2000] have proposed that reconnection is possible in the absence of separators and null points. In this scenario, reconnection occurs on quasi-separatrix layer field lines that carry a parallel electric field through a process they call magnetic flipping. Furthermore, researchers have developed and tested the theory for reconnection at current-carrying magnetic null points [*Galsgaard and Pontin*, 2011a, 2011b;

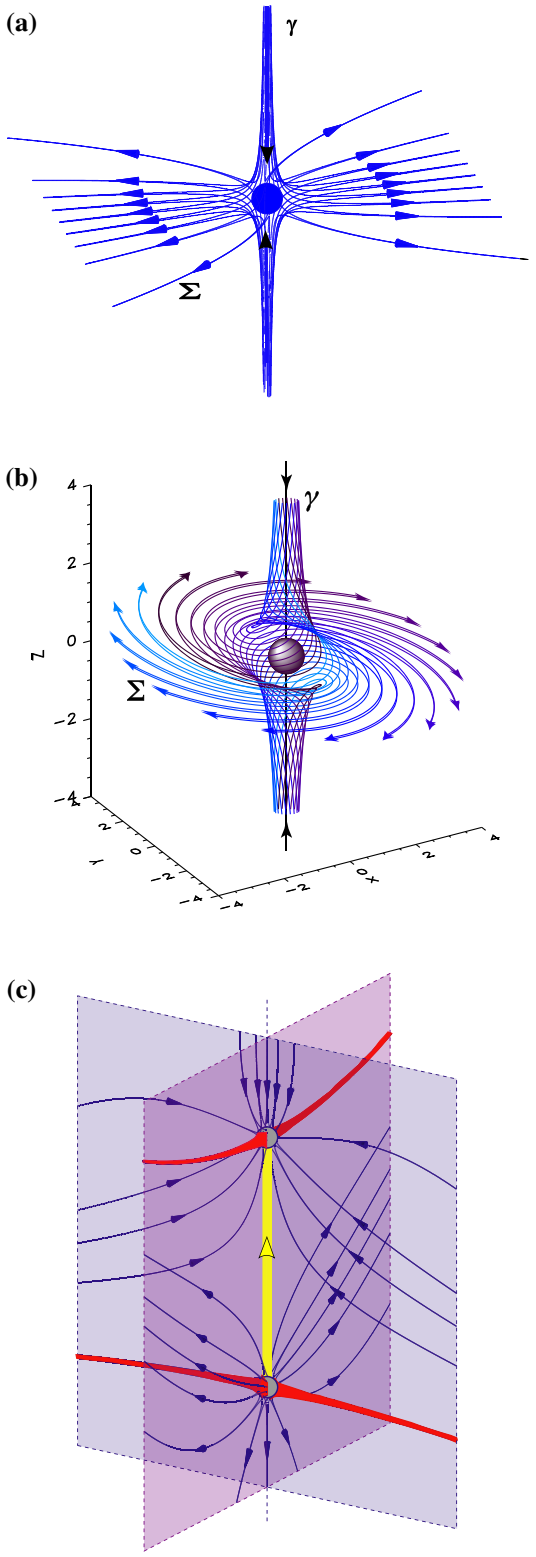

Figure 1. (a) Spine γ and fan plane Σ of an improper radial null point. (b) Type B_s spiral null point. (c) Intersection of the fan planes (shaded surfaces) of a type A and a type B radial null point defines the separator (yellow line). Figures 1a and 1c are based on Figure 1 from *Pontin* [2011].

Pontin and Galsgaard, 2007; *Pontin et al*., 2005a; *Pontin et al*., 2007; *Pontin et al*., 2011; *Priest and Titov*, 1996; *Priest and Pontin*, 2009; *Wyper and Jain*, 2010], while others [*Bogdanov et al*., 1994; *Lukin and Linton*, 2011] have observed null point current growth and reconnection in the laboratory. *Priest and Pontin* [2009] deduce three general categories of null point reconnection: torsional spine, torsional fan, and spine-fan reconnection. In torsional spine reconnection, when current concentrates along the spine from field lines rotating in the fan plane, nearby field lines can experience rotational slippage, i.e., elements of the field lines at different positions along the spine rotate at different rates, thereby separating plasma elements along parts of the spine from their original field lines. Torsional fan reconnection occurs when spine field lines rotate in opposite directions above and below the fan, building up current within the fan and forcing field lines near the fan to rotate in opposite directions above and below the fan. However, there is no flux transfer across either the spine or the fan in either of these models. Finally, in spine-fan reconnection, a shearing motion across the spine causes the null point to collapse into a current sheet and flux is transported across both the spine and the fan [*Parnell et al*., 1997; *Priest and Pontin*, 2009].

[8] In this article, we initiate a new approach that applies a 3-D analysis to filamentary currents in turbulent geospace. In previous analyses of a 2002 Cluster magnetosheath crossing, *Retinò et al*. [2007] find filamentary current sheets and evidence for reconnection and dissipation, while *Sundkvist et al*. [2007] establish that the layer is turbulent. Using the Cluster magnetic field data, we apply multispacecraft topological analyses to current sheets observed during this time interval to discover magnetic nulls associated with many of the current filaments. In particular, we examine a pair of nulls that may be topologically connected. Because the current layers cross the spacecraft and the mean magnetic field fluctuates in about 1 s or less, particle moments are not useful during this interval. We therefore rely on electric fields outside the dissipation region to infer neighboring plasma flows in the null rest frame. We find that the pair of nulls manifests a current structure and flow pattern consistent with at least one type of null point reconnection—torsional spine reconnection—discovered in a number of theoretical works [*Pontin et al*., 2007; *Pontin et al*., 2011; *Priest and Titov*, 1996; *Priest and Pontin*, 2009; *Wyper and Jain*, 2010].

2. Topological Analysis

[9] On 27 March 2002, from about 9:30 to 11 UT, the Cluster spacecraft passed downstream of a quasi-parallel shock through a turbulent magnetosheath filled with thin current layers [*Retinò et al*., 2007]. At this time, Cluster's orbit passes near the southern cusp on the dawn side of noon (about 10 magnetic local time). The spacecraft tetrahedron is highly regular, and the interspacecraft spacing is about 100 km. The flux gate magnetometer (FGM) B_x component from Cluster 1 (Figure 2a) with 0.015 s cadence shows the highly filamentary nature of the field, associated with many thin current sheets. *Retinò et al*. [2007] analyze a current sheet with a very depressed magnetic field and high ohmic dissipation at about 10:16:52 UT. They find a field reversal and drift flows consistent with magnetic reconnection. However, the quasi 2-D dependence of the magnetic field and currents during the interval did not readily lend themselves to a 3-D topological analysis.

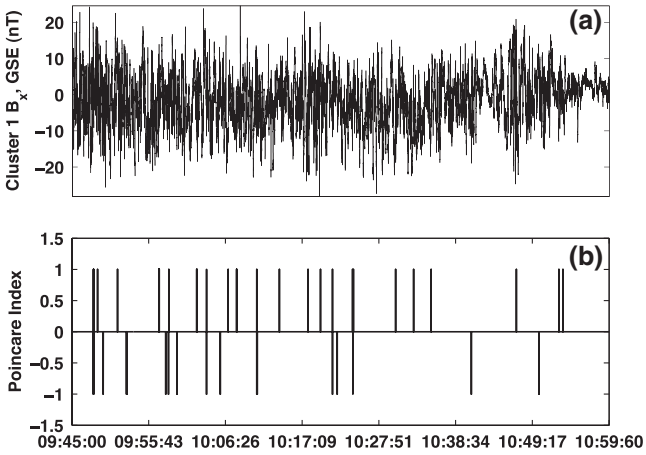

Figure 2. (a) The GSE x component of the magnetic field from the FGM instrument on Cluster 1 shows fluctuations and discontinuities of the magnetic field in the magnetosheath. (b) The Poincaré index calculated from all four spacecraft field measurements from the same time interval reveals a number of clusters of magnetic nulls entrapped within the tetrahedron.

[10] In an effort to gain insight into the dimensionality of some of the current sheets, we apply a few magnetic gradient analyses to the FGM data from this interval. Cluster four-point measurements yield the magnetic spatial gradients averaged over the tetrahedron [*Chanteur*, 1998; *Dunlop et al*., 2002], from which one derives the current. Large spatial gradients signify strong currents. The spacecraft four-point position and magnetic field data also provide the so-called topological degree, or Poincaré index, a measure of the number of roots—in the case of interest, magnetic nulls—in a region [*Greene*, 1992]. The origin, or root, in magnetic field space corresponds to a magnetic null point in configuration space. The field in the linear region near a null may be expanded as $\mathbf{B} = \nabla\mathbf{B}\cdot\mathbf{r}$, where $\nabla\mathbf{B}$ is the matrix of magnetic spatial gradients $\partial B_i/\partial x_j$ evaluated at the null. The eigenvalues of $\nabla\mathbf{B}$ correspond to the nature of the spine and fan of the null. If all three eigenvalues are real, the null is a type A or type B radial null. In this case, the eigenvalue λ_γ corresponding to the spine γ is of opposite sign to the other two eigenvalues, and its sign determines whether the spine points toward ($\lambda_\gamma < 0$) or away ($\lambda_\gamma > 0$) from the null. If one eigenvalue is real and the other two complex conjugates, then the null is a type A_s or type B_s spiral null and the sign of the real eigenvalue gives the orientation of the spine. Because the determinant of the matrix is the product of the eigenvalues, its sign specifies the polarity of the null. The topological degree $\mathbf{D}$ is given by $\mathbf{D} = \Sigma\ nulls\ \mathrm{sign}(\det(\nabla\mathbf{B}))$ and represents a sum of like-type magnetic nulls in a given region (and will vanish if the region contains a pair of opposite nulls).

[11] One method of calculating the topological degree is the bisection method of *Greene* [1992], whereby knowledge of the magnetic field at specific points over a volume in configuration space allows a mapping between configuration (x, y, z) and magnetic field (B_x, B_y, B_z) space [*Dorelli et al.*, 2007]. From this information, one calculates the solid angle subtended in magnetic field space by the volume in physical space. The total solid angle thus subtended is either 0 or a

multiple of 4π, depending on whether the origin in magnetic field space ($\mathbf{B} = 0$) is enclosed. Of course, enclosure of nulls of opposite polarity will have a topological degree of zero, so the topological degree measures the number of enclosed isolated nulls. The magnetic field measurements on the triangular surface of the Cluster tetrahedron provide solid angles in magnetic field space. One projects these onto the unit sphere in magnetic field space to evaluate the topological degree. Several researchers have previously applied this method to detect the entrainment of magnetic nulls by the Cluster spacecraft [*Deng et al*., 2009; *He et al*., 2008; *Xiao et al*., 2006] in the magnetotail.

[12] After applying the bisection method to the time interval of the turbulent magnetosheath, we find an abundance of entrapped magnetic nulls, as evidenced by the Poincaré index in Figure 2b. There may be many more nulls than are actually caught within the spacecraft tetrahedron. As we shall show, many of these nulls are associated with strong currents. Furthermore, many appear to be paired. As proposed by *Albright* [1999] and observed by *Parnell et al*. [2007, 2008] and others in solar data, many seem to cluster. Since Cluster has only four facets, the method as implemented is not as robust as envisioned by Greene, who uses a dodecahedron to evaluate **D**. However, the regularity and small size of the tetrahedron during this interval reduces the likelihood the field varies nonlinearly over the volume. As demonstrated by *Retinò et al*. [2007], the spacecraft separation is on the order of the local ion inertial scale (~100 km). As further demonstrated by *Sundkvist et al*. [2007], the turbulent intermittency scales with the ion inertial length, indicating that magnetic nonlinearities associated with the turbulence should dissipate into the particles on these length scales. Furthermore, as discussed below, the deviation of $\nabla \cdot \mathrm{B}$ from zero provides a measure of the local nonlinearity in the gradients of the field obtained from the curlometer method, which intrinsically assumes a linear field. Though the deviation of the Poincaré index from integer values is 10^{-15}, on the level of the numerical round off, it is still possible for the bisection method to produce false positives and false negatives [*Haynes and Parnell*, 2007]. Therefore, we apply our analysis to magnetic null points observed for several consecutive snapshots to strengthen the case that the observed null points are real. Moreover, none of the indices exceeds unity, which reduces the likelihood that the linear interpolation over one of the tetrahedron surfaces is invalid [*Greene*, 1992].

[13] The results of this paper come from a detailed analysis of a pair of nulls captured between about 9:48:01 and 9:48:02 UT. We derive their topological characteristics from the matrix of magnetic spatial gradients derived from the tetrahedron geometric factors [*Chanteur*, 1998; *Dunlop et al*., 2002]. Figure 3a displays the Poincaré index of the pair of entrapped nulls that are close to one another and have opposite polarity. Each null is observed for seven consecutive time steps. The vertical dashed lines locate the peak currents at each null. Figures 3b–3d show several other of their topological quantities: the determinant of $\nabla\mathbf{B}$, whose sign corresponds to the polarity of the nulls and whose magnitude indicates the size of local currents (Figure 3b); what we call the null-type index, which is zero for complex eigenvalues, and nonzero for real eigenvalues, where it takes on the value of $\det(\nabla\mathbf{B})$—thus revealing whether the null is radial or

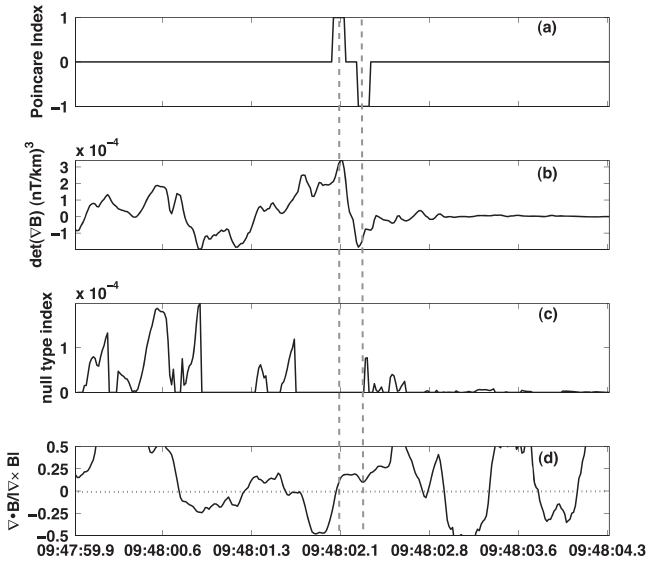

Figure 3. (a) Poincaré index, revealing a pair of oppositely polarized nulls that are the subject of this paper. (b) Determinant of $\nabla\mathbf{B}$, whose sign indicates the orientation of the magnetic field, and whose magnitude reveals the strength of the discontinuity. Large values indicate strong currents. The vertical dashed lines denote the location of the peak currents. (c) The null-type index is defined to be zero when the eigenvalues are complex and the product of the eigenvalues when the eigenvalues are real. Since the index is zero throughout most of the interval, both nulls are probably of the spiral type. (d) The quality index $\nabla\cdot\mathbf{B}/|\nabla \times \mathbf{B}|$ indicates the accuracy of the magnetic spatial gradients. In the interval surrounding the nulls, it is less than 12%.

spiral (Figure 3c); and a quality index, $\nabla\cdot\mathbf{B}/|\nabla \times \mathbf{B}|$, which estimates the quality of both the magnetic gradients and the current at a given location (Figure 3d). The pair of nulls, since they are adjacent and have opposite sign, may be magnetically linked. The Cluster tetrahedron resolves each null for several consecutive time steps, increasing confidence that the detections are robust. This fact also decreases the likelihood that the detection involves a null that is very close to one edge of the tetrahedron. A null that lies very close to an edge can increase the chance of error arising from linear interpolation along one side [*Greene*, 1992]. The determinant of $\nabla\mathbf{B}$ is consistent with the sign of the Poincaré index and shows that the first null encountered is a negative (type A or A_s) null, and the second a positive (type B or B_s) null. The null-type index reveals that the first null is a spiral A_s null. The index is somewhat more ambiguous for the second null, since a few time steps have real eigenvalues, while most of the time steps have complex eigenvalues during the enclosure of the null. The second null is therefore most likely a type B_s null, though the changing eigenvalues may imply that the null characteristics vary over the observing period.

[14] The quality factor at the leading and trailing edges of the null entrainment in Figure 3d ranges between about 10 and 20% but, in the center of the interval, is generally less than 10% and becomes very small, passing through zero at the peak gradients. The spatial gradients are determined from a least squares minimization function that exploits the

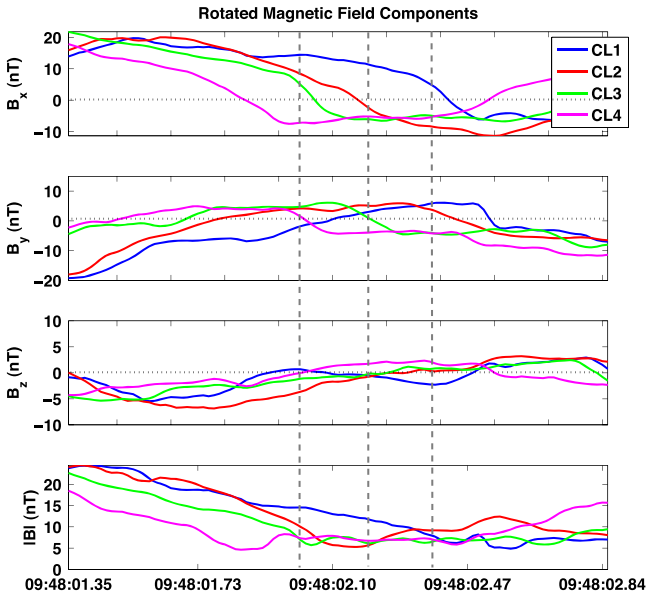

Figure 4. From top to bottom: x, y, and z components and magnitude of the magnetic field from all four spacecrafts in the LMN coordinate system.

multipoint positions and magnetic field measurements (and is sometimes referred to as the curlometer method when applied to find the current) [*Harvey*, 1998]. Because the methodology used to derive the gradients of **B** assumes a linear field over the span of the tetrahedron, the deviation of $\nabla\cdot\mathbf{B}$ from zero arises primarily from truncation errors due to the presence of nonlinearities in the field over the volume. A crude estimate of the resulting error in $\partial B_i/\partial x_j$ is $\sim 1/3|\nabla\cdot\mathbf{B}|$, which for null A_s is about 0.005 nT/km at the peak current, and for null B_s is about 0.01 nT/km at the peak current (see Table A2). The resulting truncation error relative to the dominant gradients in **B** is about 4.5% for null A_s and 2% for null B_s. Further from the null, the quality factor exceeds 50%, which probably reflects the fact that $\nabla \times \mathbf{B}$ becomes small, but also may indicate where the field surrounding the null point becomes nonlinear.

[15] Initially, we follow the path observers typically pursue when they encounter discontinuities in the magnetic field in space and neglect field variations in a third dimension. We will demonstrate the risk inherent in doing so: ignoring the field variation along the direction of the current yields an apparent Hall field structure consistent with 2-D reconnection, although the field in fact contains a 3-D null point and is highly complex. First, we perform a minimum variance analysis to find the LMN boundary normal coordinate system for the currents [*Sonnerup and Scheible*, 1998]. The currents at both nulls share a common orientation and therefore a single rotation suffices for both. The eigenvectors for this rotation are [0.4979, 0.4767, 0.7244; 0.1972, 0.7512, −0.6299; 0.8445, −0.4565, −0.2800]. Figure 4 shows the rotated magnetic field components and the magnetic field magnitude for all four spacecraft. The two nulls are located between the sets of dashed lines. (As we will show, though the nulls are separated by roughly the spacecraft spacing, their motion is such that they are not captured at the same time. However, it is possible that they are both entrapped during the brief 0.09 s interval between the null entrapments during which the Poincaré index vanishes.) First observed by Cluster 4, and then finally by Cluster 1, the maximum variance magnetic field along x in the new coordinate system changes sign, accompanied by a modest normal magnetic field of about 2 nT in the new z direction, and an intermediate variance (rotated y component) that also changes sign on most of the spacecraft. Based on this information alone, the interval bears the earmarks of a 2-D Hall current sheet: the magnitude of the magnetic field is depressed to about 5 nT, while, except for the B_y component on Cluster 2, all three field components reverse. (The three components do not necessarily reverse at the same time, but a synchronous reversal only occurs if the spacecraft crosses the center of the reconnecting structure.) However, as we already know, the complete analysis shows that the fields and currents are not 2-D. Figure 5 shows that the curlometer current components at the centroid in the LMN system lie predominantly along the $-y$ direction of the rotated system. (For a regular tetrahedron, the relative error in the current is about 10% [*Robert et al.*, 1998].) In the absence of a topological analysis, one fails to realize that the roughly 1-D current layer corresponds to a 3-D magnetic structure.

[16] To capture the instantaneous 3-D structure of the nulls in a turbulent medium, it is necessary to remove the motion of the nulls and find the positions of the spacecraft in the null rest frame. One way to achieve this is to take advantage of the proximity to the null and use a linear expansion of the fields around the null. By placing the null at the center of this coordinate system at each point in time, we produce a superposed epoch snapshot of the magnetic field structure around the null, in same the manner *Wendel and Reiff* [2009] derive a snapshot of a 2-D x-type structure around a current sheet in the magnetopause. We will show that not only does this method provide the instantaneous position of the null in absolute space but, therefore, also the velocity of the null. From the positions **r** of the spacecraft,

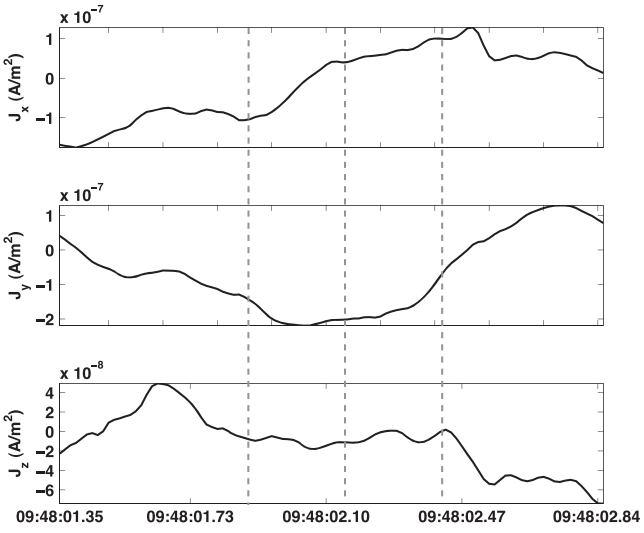

Figure 5. The x, y, and z components of the curlometer current in the LMN coordinate system surrounding the pair of nulls. The current is predominantly along y, in the same direction at both nulls, and a somewhat more modest component along x changes sign at each null.

the magnetic field measurements **B**, and the gradients of the field, we derive the null position $\mathbf{r}_0$, at each point in time the tetrahedron is near the null, through inversion of the linear expansion

$$\mathbf{B} = \nabla\mathbf{B}|_{r_0}\cdot(\mathbf{r} - \mathbf{r_0}). \quad (1)$$

[17] In practice, we could solve for $\mathbf{r}_0$ from using the magnetic field measurements and positions of whichever spacecraft is closest to the null (based on the magnitude of the magnetic field.) However, there is a problem in using the magnitude of the field, since the spacecraft are simultaneously very close to two nulls, and the field is more depressed at one null than at the other. Moreover, since there is a degree of error involved in the linear approximation, the error changes when the spacecraft used for the calculation changes. This can produce a small but artificial jump in $\mathbf{r}_0$ and hence in the null velocity $\mathbf{v}_0$ when the spacecraft that is closest changes. For these reasons, and since the gradients correspond to the centroid, we use the centroid position and magnetic field for the entire time interval. This approach is also advantageous in that we do not rely on the magnitude of the field to find the point of closest approach, but rather the magnitude of the curlometer current, which is most valid at the location of the centroid. In equation (1), the spatial gradients are evaluated at the time t_p of peak current near each null crossing to invert for the null position. Using those spatial gradients, we perform the inversion for a brief time interval (roughly corresponding to the interval between dashed lines in Figure 4) around each null to derive the instantaneous magnetic structure around each null, and the position and velocity of each null. The values for $\nabla\mathbf{B}$ in the LMN coordinate system at nulls A_s and B_s are, respectively,

$$\nabla\mathbf{B}_{A_s} = \begin{pmatrix} -0.0380 & -0.0464 & -0.2532 \\ -0.0659 & 0.0076 & 0.0227 \\ 0.0222 & 0.0128 & -0.0131 \end{pmatrix} \mathrm{nT/km}$$

$$\nabla\mathbf{B}_{B_s} = \begin{pmatrix} 0.0587 & -0.0089 & -0.2225 \\ -0.0085 & 0.0647 & 0.0730 \\ 0.0087 & 0.0030 & -0.0368 \end{pmatrix} \mathrm{nT/km.}$$

[18] Once we know $\mathbf{r}_0$ at a given time, we also know the position of each spacecraft relative to the null at $\mathbf{r}_0$. Prior to inverting, to aid in accurately capturing the null point, we filter the magnetic field data with a zero-phase forward and reverse digital IIR Butterworth band-pass filter between about 1.5 and 8 Hz. This type of filter results in zero-phase distortion and minimizes endpoint transients. The 1.5 to 8 Hz band contains wave power that might affect the position estimates but is not related to the underlying current/magnetic structure we are seeking. We retain frequencies below 1.5 Hz because this range corresponds to the timing of the underlying magnetic structure as it passes by the spacecraft (~0.7 s). Figure 6 maps the measured value of B_x in the LMN coordinate system as a function of the LMN vertical distance z of each spacecraft (color coded) from null A_s (top panel) and null B_s (bottom panel). In the absence of further topological information, the data look like a 2-D current sheet crossing. As we shall show, the "current sheet" depicted in Figure 6 is in fact a current along the spine

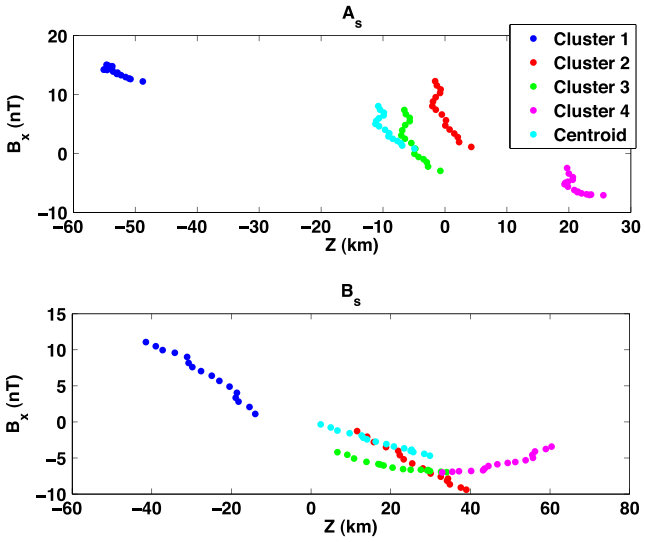

Figure 6. The superposed epoch B_x profiles as a function of distance Z across the current layer in the LMN coordinate system for null A_s, above, and null B_s, below. Data are accumulated from each spacecraft during the ~0.3 s interval crossing of each null, including averaged values calculated at the centroid. The centroid is used to identify the instantaneous position of the null.

of each null. The random errors in $\mathbf{r}_0$ (on the order of about 2–13 km) come from random errors in the components B_i and in $\partial B_i/\partial x_j$ (all summarized in Table A1), which are, respectively, 0.1 nT and 0.0014 nT/km for both null A_s and null B_s. The systematic errors in $\mathbf{r}_0$ range from a few to about 20 km for most of the interval (see Figure 17). The systematic errors owe primarily to truncation from the linear approximation for $\partial B_i/\partial x_j$, which we estimate to about 0.005 nT/km for null A_s and 0.01 nT/km for null B_s, for the values used in the inversion (summarized in Table A2). We describe the estimation of errors in detail in Appendix A. There is another source of error in assuming we are close enough to the null that the linear relation in (1) holds. While we do not attempt to quantify this error here, in section 3.1, we demonstrate that the linear approximation is reasonable over the analysis interval.

[19] From the eigenvectors and eigenvalues of $\nabla\mathbf{B}$, we derive the direction of the spine and the major fan axis in the LMN coordinate system. Following *Parnell et al.* [1996], we rotate the data into a coordinate system such that the new z' direction lies parallel to the spine and the new x' direction lies along the current perpendicular to the spine. A 2-D superposed epoch portrait of the magnetic field structure around the nulls in this new coordinate system, with the field data color coded according to spacecraft, shows the rotational fields in the fan planes, oriented at an angle to the spines (Figures 7 and 8). In Figures 7 and 8, the colored arrows represent the magnetic field vectors at each spacecraft position around the null, which is placed at the center of the coordinate system. The black vectors represent the current. The top panel provides a view along the normal to the plane defined by the spine and the perpendicular current (x' and z'), and the bottom panel shows a view along the spine of the plane perpendicular to the spine. The spiral

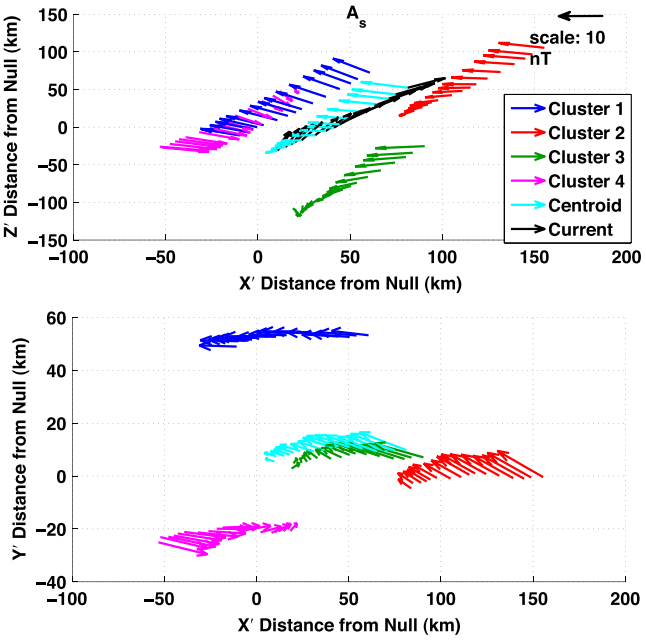

Figure 7. Two views of a superposed epoch of the magnetic field vectors from all four spacecraft and the centroid surrounding null A_s in the spine-aligned coordinate system. The black arrows in the top view represent the current at the location of the centroid. The top view is along the normal to the plane defined by the spine (along z') and the perpendicular current (along x'). The bottom panel is a view along the spine of the plane perpendicular to the spine, which reveals the spiral nature of the field lines around the spine. The current is mostly spine aligned but has a component perpendicular to the spine as well.

nature of null A_s is clearly evident in the bottom panel of Figure 7. While the B_s field lines in Figure 8 are also consistent with a spiral, they appear to have a larger radius of curvature than those of A_s. Also apparent are the outward orientation of the spine of A_s and the inward orientation of the spine of B_s. To clarify the orientation of the spines and the fans, Figure 9 is a view along the normal to the x'–z' plane of the eigenvectors of the spine (blue arrows) and one of the major fan axes (red arrows) at each location of the centroid as it passes near the null. In the case of complex fan eigenvectors $\mathbf{e}_\Sigma$, the fan plane is defined by $\mathrm{Real}(\mathbf{e}_\Sigma) \pm \mathrm{Im}(\mathbf{e}_\Sigma)$. The minimum angle between the spine and the fan is about 23° for null A_s and about 45° for null B_s, as determined by the angle between the spine and the normal to the fan plane. However, the angle between the spine and the particular fan vector depicted in Figure 9 is about 45° for null A_s and 77° for null B_s.

[20] The current at a null point determines its structure. A current $J_\parallel$ along the spine produces skewed field lines in the fan plane, and a current $J_\perp$ perpendicular to the spine serves to tilt the spine toward the fan. A threshold current J_{thr} based on the magnetic spatial gradients, or, equivalently, on the eigenvalues of $\nabla\mathbf{B}$, primarily determines whether the fan eigenvectors are real or complex, and hence whether fan field lines are radial or spiral [*Parnell et al.*, 1996]. In terms of the eigenvalues, the threshold current may be expressed as

$$J_{\mathrm{thr}} = \frac{1}{\mu_0}\left[2\left(\lambda_{\Sigma_1}^2 + \lambda_{\Sigma_2}^2\right) - \lambda_\gamma^2 + \left(\mu_0 J_\parallel\right)^2\right]^{1/2}, \qquad (2)$$

where λ_Σ refers to the fan eigenvalues and λ_γ refers to the spine eigenvalue. The current observed at both nulls is largest along the spine, though there is a perpendicular component in both cases. The current along the fan planes is similar to the current along the spine, though somewhat smaller in the case of null B_s. The field rotations are in the same sense above and below the fan plane, consistent with the fact that the orientation of the spine-aligned current is the same above and below the fan plane. The perpendicular component gets stronger at null A_s farther away from the null to the point that the current is primarily along the fan. (There are not enough data at null B_s to determine if this happens there as well.) For null A_s, the current components are $J_\parallel = 0.186\ \mu\mathrm{A\ m^{-2}}$, $J_\perp = 0.112\ \mu\mathrm{A\ m^{-2}}$, and $J_{\mathrm{thr}} = 0.163\ \mu\mathrm{A\ m^{-2}}$, and for null B_s they are $J_\parallel = 0.185\ \mu\mathrm{A\ m^{-2}}$, $J_\perp = 0.058\ \mu\mathrm{A\ m^{-2}}$, and $J_{\mathrm{thr}} = 0.174\ \mu\mathrm{A\ m^{-2}}$. Thus, $J_\parallel$ exceeds J_{thr} at both nulls, consistent with spirals. Because of the values for the current components and J_{thr}, these nulls correspond to the case **VC2** in *Parnell et al.* [1996]. The current J_Σ within the fan plane of null A_s is about the same as that of $J_\parallel$, which means that the net current is oriented halfway between the spine and the fan. $J_\perp$ is larger at null A_s than at null B_s, in accordance with a more highly tilted fan plane. A current along the spine is generically consistent with torsional spine reconnection, while the current within

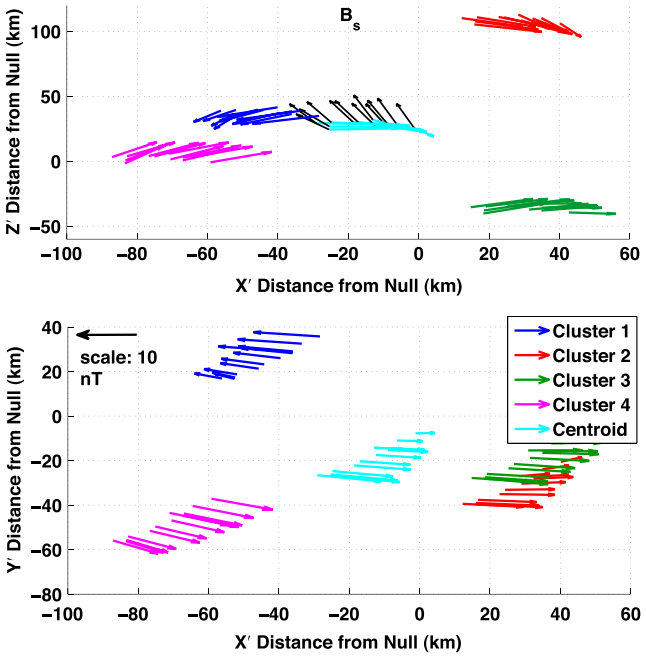

Figure 8. As in Figure 7, two views of the magnetic vector fields and the current surrounding null B_s. The fields appear to be also rotating around null B_s, though they are not as tightly wound as those around null A_s. The orientation of the spine into the null from above and below is consistent with the field lines in the top panel. Again, the current is primarily along the spine, in the same sense as null A_s, but also has a component perpendicular to the spine, in the opposite sense to null A_s.

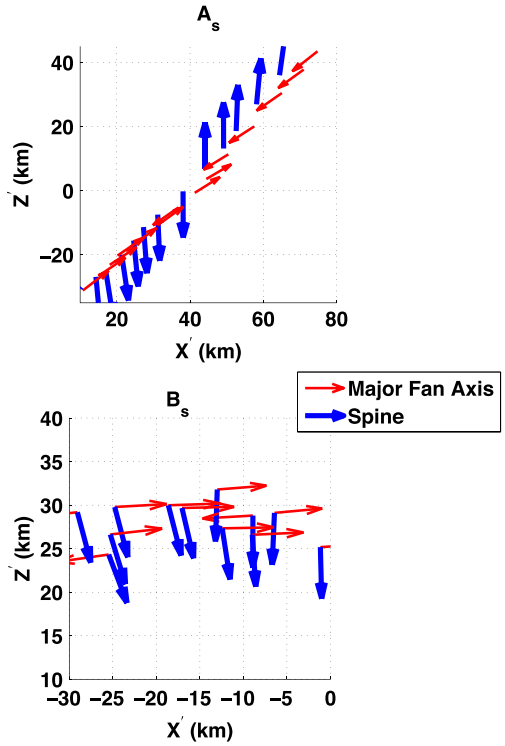

Figure 9. A superposed epoch of the spine (blue arrows) and fan (red arrows) eigenvectors at the position of the centroid around null A_s (above) and null B_s (below). The view is along the normal to the spine (along z') and the perpendicular current (along x').

the fan is consistent with torsional fan reconnection. Table 1 summarizes the null characteristics discussed so far (as well as some we shall discuss in the following sections). Some quantities are presented in both the spine-aligned and the LMN coordinate system, as noted. Like the magnetic gradients chosen for the derivation of $\mathbf{r}_0$, the stated eigenvalues and eigenvectors are evaluated at the time of peak current.

3. Velocities

3.1. Null Velocities

[21] Reconstruction of the relative positions of nulls A_s and B_s and transformation of drift flows (derived from the fields) into the null rest frame both require the null point velocity $\mathbf{v_0}$, which we obtain directly from the derivative of $\mathbf{r}_0(t)$. This method for determining $\mathbf{v}_0$ assumes stationary fields in that $\nabla\mathbf{B}$ is held at a fixed value for all time steps because of the linear Taylor expansion about a fixed point (the null point). Because all four spacecraft observe very similar magnetic fields during the interval surrounding the nulls, we assume that the interval is reasonably stationary. However, the inversion of equation (1) also assumes a linear field. Therefore, it is useful to compare this method of finding $\mathbf{v}_0$ to an existing method that, although likewise assuming linear gradients and quasi-stationarity, does not assume a linear expansion of the field about a fixed point. Therefore, we also derive $\mathbf{v_0}$ by the method of *Shi et al.* [2006]. This method relies on the assumption that the structure is quasi-stationary so that the relation

$$\frac{d\mathbf{B}}{dt} + \mathbf{v}_0 \cdot \nabla\mathbf{B} = \mathbf{0} \tag{3}$$

is satisfied. Other caveats apply to spatial and temporal scales, owing primarily to the truncation errors in the linear approximation for $\nabla\mathbf{B}$. The spatial constraints are that the size of the overall structure should exceed the spacecraft spacing and that the gradient in B_i in any given direction should exceed the ratio of the uncertainty in B_i to the spacecraft spacing along that direction. The time over which the structure moves across the spacecraft spacing should exceed the time step used in the calculation. At the same time, the time step used in the calculation should exceed the ratio of the uncertainty in B_i to the rate of change of B_i. The data during this interval satisfies the above criteria. If we assume $\mathbf{r}$ is approximately constant in equation (1), the derivative of equation (1) is almost equivalent to equation (3), except that equation (3) does not assume an expansion about a point. Therefore, in equation (3), $\nabla\mathbf{B}$ is evaluated at each point in time. By dint of this difference in deriving $\mathbf{v}_0$ from the derivative of equation (1) and from equation (3), results from the two methods provide a way of gauging the validity of the linear expansion in equation (1).

[22] From Figure 10, which shows the velocities in the LMN coordinate system derived using both the superposed epoch and the *Shi et al.* [2006] methods at null B_s, we see that the methods agree very well. The superposed epoch method, based on the gradient at the time of peak current, gives a $\mathbf{v}_0$ that agrees very closely with that from the magnetic time derivative. The good comparison provides an estimate of the validity of the fixed-gradient Taylor expansion about the null point in the analysis interval. We find from the mean values of the components over the interval that, in the LMN system, $<\mathbf{v}_0>$ = [−106, −300, −28] km/s for null A_s, and $<\mathbf{v}_0>$ = [−150, −52, −117] km/s for null B_s. (Note that we shall refer to the null position and velocity in the spine-aligned coordinate system as $\mathbf{r}'_0$ and $\mathbf{v}'_0$, respectively.) The errors in $\mathbf{v}_0$ are dominated by the systematic truncation errors in the estimation of $\mathbf{r}_0$ and are summarized in Table A2. They represent a potential systematic bias $\delta\mathbf{v}_0$ so that the true velocity may lie anywhere from the stated value to the stated value plus $\delta\mathbf{v}_0$. In LMN coordinates, they are $\delta\mathbf{v}_0$ = [90, −158, 20] km/s for null A_s and $\delta\mathbf{v}_0$ = [56, −33, 14] for null B_s. Though these values may at first seem significant, we shall see in the following section that they do not affect the final results for the plasma flow around the null in any qualitative way. The random error bars $\delta\mathbf{v}_{0,\mathrm{rms}}$, summarized in Table A1, come from statistical uncertainties in B_i and $\partial B_i/\partial x_j$ in the calculation of $\mathbf{r}_0$ and from statistical uncertainty in the time step dt. For null A_s, $\delta\mathbf{v}_{0,\mathrm{rms}} = \pm$[12.95, 77.02, 11.08] km/s, and for null B_s, $\delta\mathbf{v}_{0,\mathrm{rms}} = \pm$[9.26, 5.78, 8.67]. We discuss the derivation of these and all other sources of error in detail in Appendix A.

[23] From the positions $\mathbf{r}_0$ and velocities $\mathbf{v}_0$ for each null as it overtakes the spacecraft, it is possible to make a rough portrait of the relative positions of the nulls and their relation to the spacecraft position. At t_p, the time of maximum current in the interval where the null is captured, the position of null A_s is [−2.9955, 0.5600, 9.2042] × 10^4 km (in LMN), and the corresponding position of null B_s when it is captured is [−3.0015, 0.5646, 9.2015] × 10^4. Given the velocity of null A_s, this means that, at the time B_s is captured, A_s has moved approximately $d\mathbf{r}$ = [−23.85, −67.5, −6.3] km, and

Table 1. Magnetic Null Characteristics

Characteristic	A_s Null	B_s Null	Units
Time interval of capture	9:45:03.509–9:45:03.732	9:45:03.822–9:45:03.985	h:min:s
Poincaré index	1	−1	
Null type	3-D nonpotential negative spiral, $J_{\parallel} > J_{\mathrm{thr}}$	3-D nonpotential positive spiral, $J_{\parallel} > J_{\mathrm{thr}}$	
$\nabla\cdot\mathbf{B}$ at t_p	−0.014	0.031	nT
$\nabla\cdot\mathbf{B}/\lvert\nabla\times\mathbf{B}\rvert$ at t_p	−0.05	0.12	
Eigenvalues	0.0506 $-0.0253+0.0597i$ $-0.0253-0.0597i$	−0.0662 $0.0331+0.0388i$ $0.0331-0.0388i$	nT/km
Eigenvectors (LMN)	$e_y=\begin{pmatrix}-0.477\\0.879\\-0.019\end{pmatrix}$, $e_{\Sigma1}=\begin{pmatrix}0.687\\0.301+0.598i\\-0.063+0.275i\end{pmatrix}$, $e_{\Sigma2}=\begin{pmatrix}0.687\\0.301-0.598i\\-0.063+0.275i\end{pmatrix}$	$e_y=\begin{pmatrix}0.016\\0.999\\-0.031\end{pmatrix}$, $e_{\Sigma1}=\begin{pmatrix}0.969\\-0.057+0.143i\\0.055-0.186i\end{pmatrix}$, $e_{\Sigma2}=\begin{pmatrix}0.687\\-0.057+0.143i\\0.055+0.186i\end{pmatrix}$	
Eigenvectors (spine aligned)	$e_y=\begin{pmatrix}0.000\\0.038\\-0.999\end{pmatrix}$, $e_{\Sigma1}=\begin{pmatrix}0.800\\0.160+0.244i\\0.125-0.509i\end{pmatrix}$, $e_{\Sigma2}=\begin{pmatrix}0.800\\0.160-0.244i\\0.125+0.509i\end{pmatrix}$	$e_y=\begin{pmatrix}0.000\\-0.091\\-0.996\end{pmatrix}$, $e_{\Sigma1}=\begin{pmatrix}-0.966\\-0.085+0.181i\\0.086-0.141i\end{pmatrix}$, $e_{\Sigma2}=\begin{pmatrix}-0.966\\-0.085-0.181i\\0.086+0.141i\end{pmatrix}$	
J_{thr}	0.163	0.174	μA/m^2
$\lvert J_{\parallel}\rvert$	0.186	0.185	μA/m^2
$\lvert J_{\perp}\rvert$	0.112	0.058	μA/m^2
$<\mathbf{v}_0>$ during capture (LMN)	[−106, −300, −28]	[−150, −52, −117]	km/s
$\mathbf{r}_0$ at t_p during capture (LMN)	$[-2.9955, 0.5600, 9.2042]\times10^4$	$[-3.0015, 0.5646, 9.2015]\times10^4$	km
∠ spine and fan	23	45	°
Flow type	Spiral ⊥ spine; ∥ spine, toward fan	Possible spiral ⊥ spine; ∥ spine, toward fan	

therefore, at this time, the distance between A_s and B_s is approximately $\mathbf{r}_{0,\mathrm{As}}-\mathbf{r}_{0,\mathrm{Bs}}=[41.5, -113.5, 20.7]$ km. Since the spacecraft is initially in the $-y$ direction of both nulls, and null A_s is moving faster along the $-y$ direction than null B_s, the spacecraft observes null A_s first. The spacecraft velocities are negligible compared to the null velocities. Figure 11 provides two views in the spine-aligned coordinate system of the superposed epoch of both nulls simultaneously, as they would be located at the time that null B_s (placed at the origin) is captured. Once again, the arrows are the fields measured by each spacecraft, where dark blue arrows are associated with spacecraft positions derived around null A_s, and red arrows are associated with spacecraft positions derived around null B_s. The top panel provides a view along the normal to the x'–z' plane, and the bottom panel provides a view along the spine of the plane perpendicular to the spine. It is possible that the fan field lines emanating away from null B_s wind into null A_s. To get a better grasp of the possible connectivity between the nulls, we evaluate the angles between the fans of each null, the spines of each null, and the spine and fan of both nulls (summarized in Table 2). The classic picture of topologically connected nulls depicts the spine of one null lying in the fan plane of the other null, and their fan planes then intersecting along a separator. In our case, the spines of each null are almost parallel (lying only 6° apart), but the fans are tilted at different angles from the spines so that the angle between the fans is 25°. It should be noted that the null A_s field lines, currents, and positions appear slightly modified from how they appear in Figure 7, because in Figure 11, we have used the null B_s spine-aligned coordinate system for both nulls.

[24] The topological relationship between the null points is relevant to the question of topological stability and current closure. Figure 12 is a schematic field line tracing representing the orientations, positions, and topological features of the two nulls simultaneously, again captured at their relative positions at the instant null B_s is isolated. We trace the field lines from the expression

$$\mathbf{x}(t) = C\exp(-2\gamma t)\mathbf{e}'_1 + \exp(\gamma t)R\cos(\Theta t + vt)\mathbf{e}'_2 - \exp(\gamma t)R\sin(\Theta t + vt)\mathbf{e}'_3 \quad (4)$$

[*Haynes and Parnell*, 2007]: where, γ and v are the real and imaginary parts, respectively, of the complex eigenvalues $\gamma \pm iv$, the spine eigenvalue is -2γ, and e'_2 and e'_3 are the real and imaginary parts of the complex eigenvectors e_2 and $e_3 = e'_2 \pm ie'_3$. While the null eigenvalues, eigenvectors, and positions are determined from the data, the field line tracings

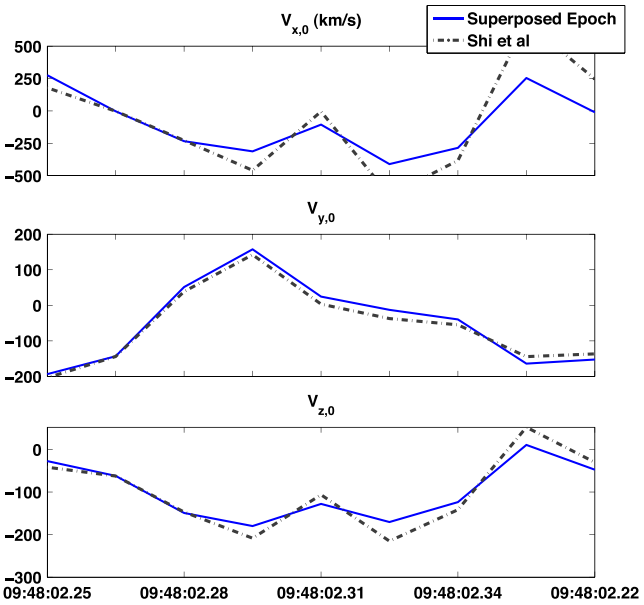

Figure 10. Null velocity profile for null B_s as determined by two methods: from the derivative of the superposed epoch position and from the method of *Shi et al*. [2006], based on the time derivative of stationary magnetic structures. The results of the two methods agree very well. The difference between the two results gives an estimate of the degree of nonlinearity of the field around the null.

provide a theoretical extrapolation over a larger region than the spacecraft can directly measure. In expression (4), $x(t)$ represents the field line, t is the position along the field line, and C, R, and Θ are constants that correspond to and define each field line. The figure shows the field lines traced for Θ equal to 0 and π radians, for fixed values of R and C. The depth of color signifies the value of Θ. The field line corresponding to $\Theta = \pi$ twines the null more loosely and appears as a distinctive dark blue or yellow line at each null. Inset (a) shows the pair of nulls from an alternate vantage point that reveals that the nulls are displaced and are not connected along their spines, which would be topologically unstable to small perturbations, while inset (b) depicts a hypothetical conception of how the nulls might connect through a common fan line (or lines).

[25] Because the fans are not perpendicular and the spines are nearly parallel, the fan field lines must undergo a nonlinear deformation at a certain distance from the null in order for the fans to intersect along a common field line. Figure 12b shows a side view of a pair of opposite polarity nulls where the spines are almost parallel and the fan surfaces curve further away from the null points. The diamonds denote sinks and the crosses denote sources, the nulls (circles) thus produced by a pair of bipolar sources. Figure 12b depicts a way that the fans of a null A_s and null B_s pair with parallel spines could intersect along a separator. This type of domed fan structure is known to exist between pairs of prone nulls on the solar photosphere and even at the Earth's northern and southern cusps, produced, for example, by fields from a pair of bipolar sources (see, for example, *Beveridge et al*. [2002]). If, as depicted in Figure 12b, a pair of opposite polarity nulls results from a pair of bipolar sources where fan field lines at each null connect to different sources (or sinks), then the domed fan surfaces intersect along a separator. (By contrast, if all the fan field lines of a given null connect to a single source (or sink), then the fans do not intersect along a separator [*Beveridge et al*., 2002].) The separator is shown as a purple curve in Figure 12b. The blue lines are fan field lines that connect null B_s to two different sinks, and the red lines depict fan field lines that connect null A_s to two different sources. Therefore, though the spines of the pair of nulls of this study point only 6° apart, conceivably they can connect along a separator, given an appropriate configuration of sources.

[26] A related question is whether the additional component of current perpendicular to the spine (and hence along the fan plane) closes the current of the null points. In a low-β or low-pressure gradient plasma, such as the solar corona, force balance constrains the current to lie parallel to the field lines [*Cowley et al*., 1997; *Lau and Finn*, 1990]. However, the magnetosheath plasma during the interval of this study has a moderate to high β of the order of unity or greater. Therefore, current closure is not constrained to lie along field lines connecting the nulls. (Indeed, therefore, the plasma β is consistent with the fact that a perpendicular current exists at the null. Because the tilt produced by $\mathbf{J}_\perp$ does not necessarily

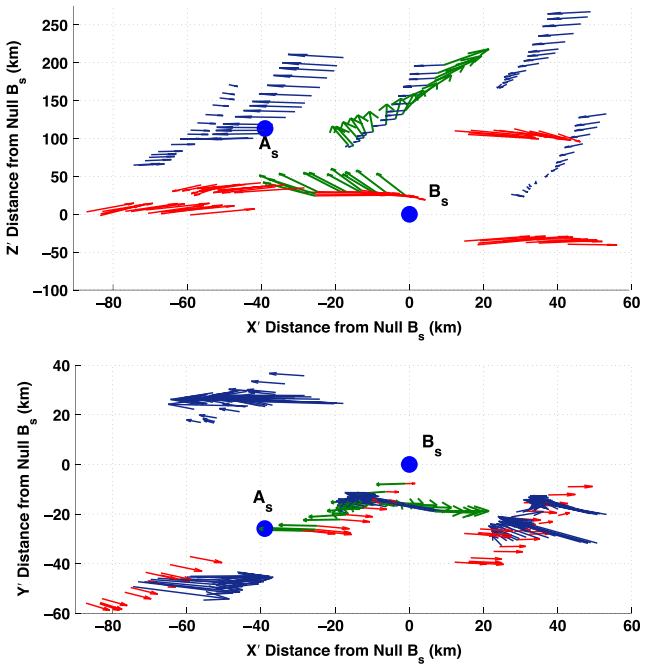

Figure 11. Two views (as in Figures 7 and 8) of the superposed epoch of the pair of nulls (depicted as blue circles) at their relative positions at the time null B_s is captured. The field lines corresponding to null A_s are shown in dark blue, and those belonging to null B_s in red. The coordinate system in this case is the spine-aligned system of null B_s. The field lines suggest that it is possible that the nulls are topologically connected. The green arrows signify the curlometer current at the position of the centroid. The reader should note that the A_s current, field line structure, and positions may appear somewhat shifted from those in Figure 7, because in this figure they are portrayed in the spine-aligned coordinate system of null B_s as opposed to that of null A_s.

Table 2. Angles Defining Null Orientations

	Angle (°)
Spine A_s and fan B_s	40
Spine B_s and fan A_s	29
Fan A_s and fan B_s	25
Spine A_s and spine B_s	6

tilt the fan about the direction of $\mathbf{J}_\perp$, $\mathbf{J}_\perp$ does not necessarily lie within the fan [*Parnell et al.*, 1996].) Though it is not clear how the current observed in Figure 11 closes, the current direction is not inconsistent with a current connecting the two null points, possibly along one of the loops portrayed in Figure 12b joining the nulls and the sources. Another possible scenario is that the null points are embedded in a larger current sheet, directed along the spines, while the current along a separator joins the two nulls.

3.2. Plasma Flows

[27] Transforming the electric field data from the Electric Fields and Waves (EFW) instrument to the rest frame of the nulls yields the drift velocities in the vicinity of the nulls. During this interval, EFW samples at 2.2 ms. We then downsample and interpolate the EFW data onto the common time tags at the FGM cadence so as to calculate the drift speeds $\mathbf{v} = (\mathbf{E} + \mathbf{E}_p) \times \mathbf{B}/|\mathbf{B}|^2$, where $\mathbf{E}$ is the field measured in the spacecraft frame and $\mathbf{E}_p = \mathbf{v}_0 \times \mathbf{B}/|\mathbf{B}|^2$ is the transformation to the null rest frame (the effect of the spacecraft velocities is negligible in comparison). The EFW instrument consists of two pairs of probes in the spin plane from which the field in the third perpendicular direction along the spin axis is found from assuming $\mathbf{E}\cdot\mathbf{B} = 0$. Though the latter assumption is clearly invalid in a diffusion region, the flows we observe do not lie within the diffusion region. As we shall discuss, it is sufficient that the flows we observe lie on field lines that thread the diffusion region closer to the spine.

[28] Because the error in the spin axis component of the field becomes prohibitively large when the angle between the spin axis and $\mathbf{B}/|\mathbf{B}|$ is less than 15° or $|\mathbf{B}| < 2$ nT [the user's guide to EFW data, Cluster Active Archive], data at these times are given a fill value. Unfortunately, for this reason, many data gaps exist during the time interval of our study, though not usually at all spacecraft simultaneously. During the interval the first null (A_s) is captured, only the Cluster 1 electric field data exist. Unfortunately, in 2001, the second probe pair on Cluster 1 failed, leaving only spin-resolution DC electric field data from Cluster 1,

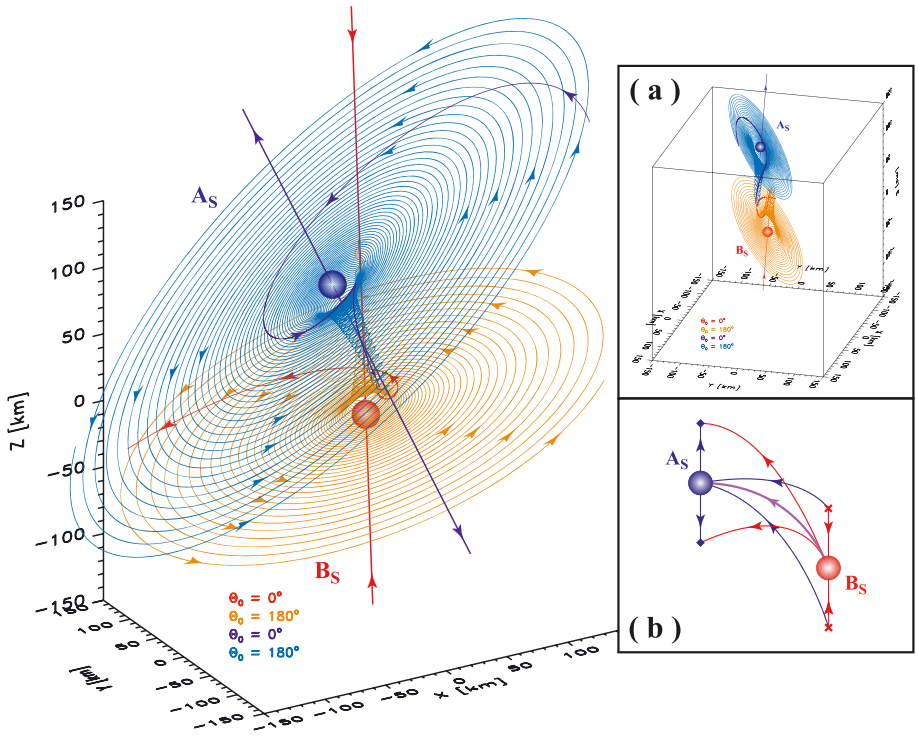

Figure 12. The fields surrounding both nulls at their relative positions at the time null B_s is captured, as traced from equation (4), based on the eigenvectors and eigenvalues of each null. Null A_s field lines are traced in blue, while null B_s field lines are traced in red. Two field lines are traced at each null, corresponding to Θ equals 0 and $\pi/2$ radians, for given values of R and C. The depth of color signifies the value of Θ. The field line corresponding to $\Theta = \pi/2$ twines the null more loosely and appears as a distinctive dark blue or yellow line at each null. Inset (a) shows the pair of nulls from a different vantage point, while inset (b) depicts a hypothetical conception of how the nulls might be connected by a common fan line (or lines). In inset (b), the nulls are shown from a side view, with the spines along the vertical axis. The nulls are produced by a pair of bipoles whose sources are denoted by crosses and whose sinks are depicted by diamonds. Each null has domed fan lines that connect to different sources (shown in blue and red) and that intersect along a common separator (shown in purple).

and clearly, spin-resolution data are inadequate to resolve the sub-second-duration current structures under consideration. However, twice per spin, the pair of probes lines up with the DC electric field in the spin plane, thus at those times accurately measuring the field. Fortunately, the interval during which Cluster captures null A_s coincides with one of those times, as we demonstrate in Figure 13. The way we establish an alignment is by looking for an agreement between the magnitude of the electric field measured by Cluster 1 and the other spacecraft approximately every 2 s (1/2 spin). For clarity, in Figure 13, we include only the Cluster 2 magnetic field magnitude, since its timing most closely matches that of Cluster 1. The gray-shaded regions highlight time intervals where the magnitudes appear to approximately agree, and these intervals occur with a periodicity of 2 s. We therefore conclude that at these times, the Cluster 1 probes are approximately aligned with the DC electric field in the spin plane and therefore accurately measure the field there. The second gray-shaded region corresponds to the interval where the tetrahedron captures null A_s. (Below, we discuss the way we estimated errors from the slight misalignment between the probe and the actual field over the 0.24 s interval.) For the interval of null B_s, as can be seen from Figure 13, Cluster 2 provides a limited set of high-quality electric field data, while none of the other spacecraft provides data during this time.

[29] Figures 14 and 15 show the resulting perpendicular flows around nulls A_s and B_s. The top two panels show two different views of a superposed epoch around the null, and the bottom panel shows the components as a function of time. The uppermost panel is a view along a normal to the plane defined by the spine and the perpendicular current, and the middle panel is a view along the spine. As detected by Cluster 1, the bottom panel shows that the flow around

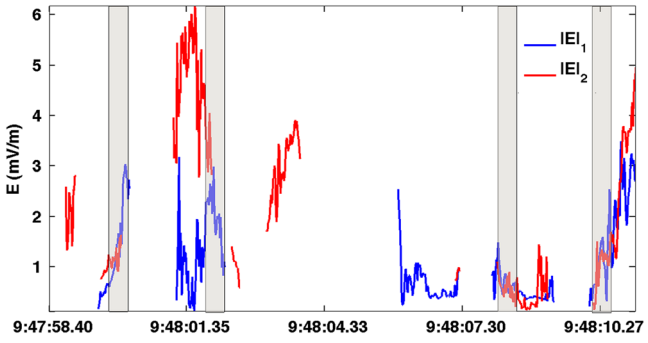

Figure 13. The magnitude of the electric field from Cluster 1 (blue) and Cluster 2 (red) over a longer interval surrounding both magnetic nulls. Gaps arise from discarding data at times where the error from the calculation of $\mathbf{E}\cdot\mathbf{B} = 0$ is unacceptably large. The gray-shaded regions denote time intervals where the magnitudes of the fields from all spacecraft match, indicating alignment of the electric probe in the spin plane with the electric field in the spin plane, which occurs every ½ spin. This analysis is necessary to verify the validity of Cluster 1 electric field data during the time interval where null A_s is analyzed, since Cluster 1 is the only spacecraft that supplies EFW data during this interval. Null A_s is captured in the time interval of the second gray-shaded region. For legibility, we include the field data from only Cluster 1 and Cluster 2, because Cluster 2 is mostly closely synchronized with Cluster 1.

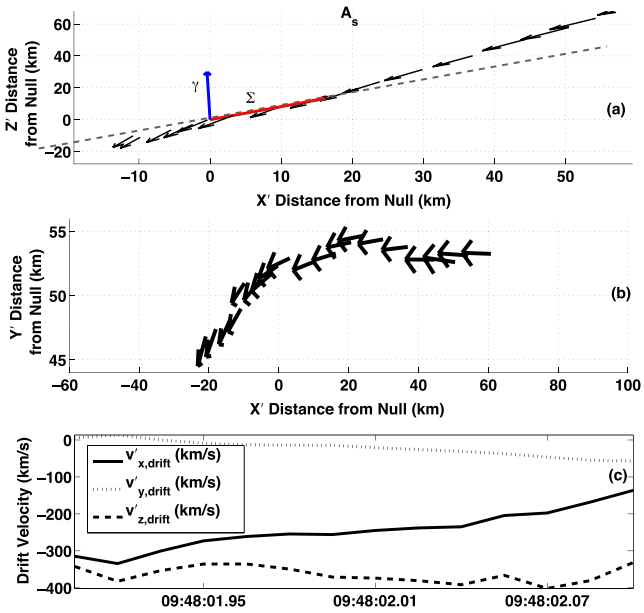

Figure 14. (a) View along the normal to the plane defined by the spine and the perpendicular current of the drift flows (black arrows) near null A_s in the null rest frame. The data are from Cluster 1 and lie at the position of Cluster 1. The blue and red arrows are the spine and fan plane, respectively. The spine and fan directions are determined at the position of the centroid at closest approach to the null but are here placed at the null. The dashed gray line is an extrapolation of the fan plane. (b) View of the same flows along the direction of the spine. The flows can be seen to rotate around the spine. (c) Corresponding magnitude of the components of the drift flows during the same time interval in the spine-aligned coordinate system.

null A_s exhibits a distinct rotational pattern around the spine in the plane perpendicular to the spine. The view from the top panel suggests that the flow is actually rotating in the fan plane. The spacecraft is, at a y' distance of ~50 km, sufficiently distant from the null as to lie outside the diffusion region and, thus, in a location where the assumption $\mathbf{E}\cdot\mathbf{B} = 0$ is valid. While the magnetic field is also rotational in this plane, the flow is still perpendicular to the field here. It is interesting to note that $\mathbf{v}$ appears to become more rotational as the spacecraft gets closer to the $z' = 0$ plane and closer to the spine. The flow pattern at null B_s is consistent with rotation in the fan plane, but the data coverage is insufficient to be conclusive. Finally, Table 1 summarizes all of the characteristics of nulls A_s and B_s.

[30] Tables A1 and A2 summarize the random and systematic errors that enter into the calculation of $\mathbf{v}$. The random errors that propagate into errors in $\mathbf{v}$ include uncertainties in $\mathbf{v}_0$, B_i, and E_i. We find two dominant random uncertainties in E_i, i.e., the misalignment of the spin-plane probe with the direction of the DC field in the spin plane, as discussed above, and the error in the spin axis alignment (as discussed in the user's guide to the EFW data, the Cluster Active Archive). In LMN, the latter is estimated to be $\pm[0.36, -0.31, -0.14]$ mV/m for null A_s and $\pm[0.06, -0.05, -0.02]$ mV/m for null B_s. In Appendix A, we discuss in detail the derivation of the former and find that it comes to $\pm[0.04, -0.03, 0.18]$ mV/m for null A_s (this error comes from the estimate of the alignment

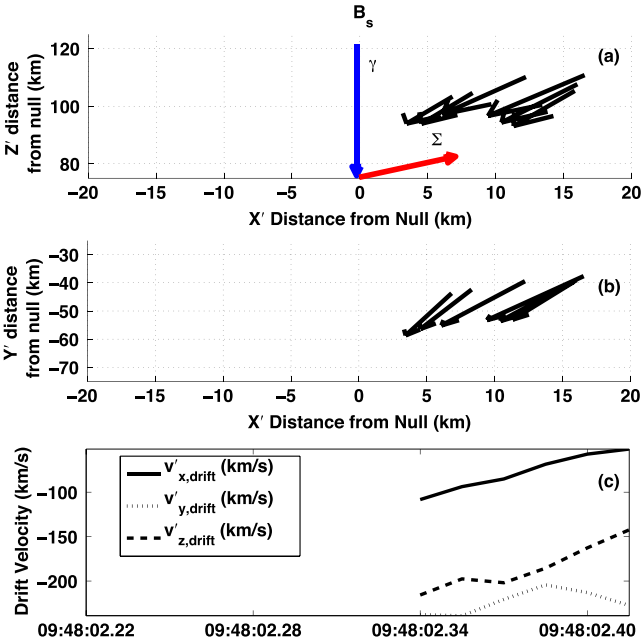

Figure 15. Drift flows for null B_s equivalent to Figure 14 for null A_s. The field data and positions correspond in this case to Cluster 2. Although the flows are consistent with rotation around the spine, the data coverage is insufficient to unequivocally verify the true nature of the drift flows.

of the Cluster 1 probe with the spin-plane field, and therefore affects only the calculation at null A_s.) We find that the net random error $\delta\mathbf{v}_{\rm rms}$ in the LMN coordinate system is [14.2, 80.0, 28.0] km/s for null A_s and ±[10.9, 34.3, 14.2] km/s for null B_s, and in the spine-aligned coordinate system, it is [33.0, 27.5, 74.0] km/s for null A_s and ±[10.7, 13.4, 34.7] km/s for null B_s. Since the spine lies along the z' axis, we see that the largest random error lies along the spine direction, which does not impact the rotational flow perpendicular to the spine. At either limit of $\mathbf{v} \pm \delta\mathbf{v}_{\rm rms}$, the qualitative nature of the flows around the nulls remains unchanged. The major systematic error once again arises from the contribution of the truncation error to the calculation of $\mathbf{v}_0$. When we adjust $\mathbf{v}$ to account for the extreme-most systematic error $\delta\mathbf{v}_0$, again the qualitative, rotational pattern to the flow remains unchanged. Figure 17 shows the time series for the adjusted components of $\mathbf{v}$ and the corresponding truncation errors in $\mathbf{r}_0$, and we can see that the velocity components maintain a qualitatively similar relationship to one another.

[31] Using kinematic models and simulations, several authors [*Pontin et al.*, 2004; *Priest and Pontin*, 2009; *Wyper and Jain*, 2010] have explored torsional spine reconnection for several initial conditions. Assuming a cylindrical diffusion region centered about the spiral null, the solution for $\mathbf{v}$ from the generalized Ohm's law, i.e.,

$$\mathbf{v}_\perp = \frac{(\mathbf{E} - \eta\mathbf{J}) \times \mathbf{B}}{B^2} \tag{5}$$

produces a rotational flow about the spine [*Pontin et al.*, 2004]. In equation (5), $\mathbf{J}$ is the current, η is the localized resistivity model, and $\mathbf{E}$ is a nonideal electric field. In the static case, $\mathbf{E}$ can be expressed as $\mathbf{E} = -\nabla\Phi$, with Φ a scalar potential. The solution to equation (5) is local in the sense that only the field lines that thread the diffusion region (imagined as a cylindrical volume around the null point) experience a change in potential Φ, while field lines that do not pass through the region have constant Φ. Thus, on field lines that have not passed through the diffusion region, both $\mathbf{E}$ and $\mathbf{v}_\perp$ are zero (assuming there is no background ideal flow). Because the diffusion region is localized about the spine, there is also a potential drop in the radial direction perpendicular to the spine. Figure 16 demonstrates the physical features of the model, where the null field lines (black curves) pass through the diffusion region (shaded cylinder). The component of the drop in potential, or electric field (blue arrow), perpendicular to the null field lines as they exit the diffusion region induces a flow (red arrows) perpendicular to it and to the magnetic field. Moreover, *Pontin et al.* [2004] demonstrate that the perpendicular potential drop and, hence, the velocity profile are independent of the model for η within the diffusion region. This is because the potential drop results from the localization of the diffusion region in conjunction with the hyperbolic shape of the field lines at the null point. As *Priest and Pontin* [2009] and *Pontin and Galsgaard* [2007] explain, the reconnection is a rotational slippage—or rotational mismatching—of field lines that spread from the spine current tube through, and outward from, the diffusion region. The plasma elements above the diffusion region that share a given field line at t_0 with plasma

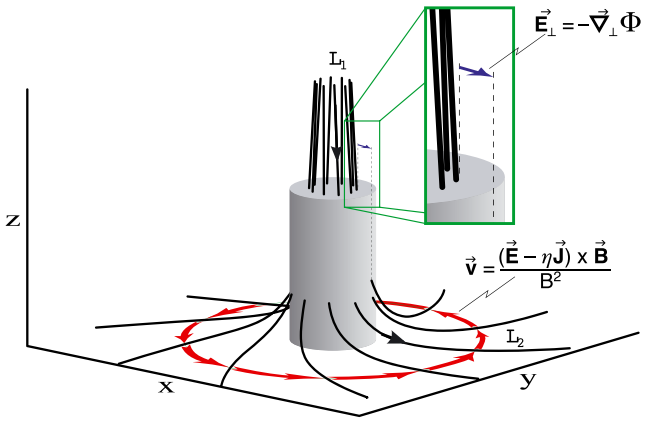

Figure 16. Field lines (black curves) that pass through the diffusion region D (shaded cylinder) encounter a nonideal potential drop $\mathbf{E} = -\nabla\Phi$ (assuming a static field) that is a function of nonideal terms, such as $\eta\mathbf{J}$, in the generalized Ohm's law. The figure shows the perpendicular component of $\mathbf{E}$ that contributes to a perpendicular velocity $\mathbf{v}$ in the fan plane outside the diffusion region. For the field lines that pass through D, the solution to the generalized Ohm's law $\nabla\Phi + \mathbf{v} \times \mathbf{B} = \eta\mathbf{J}$ yields a rotational perpendicular velocity component as displayed in the figure (see equation and red arrows). On field lines that do not pass through D, $\mathbf{v}$ vanishes, since η is zero and Φ is constant. Initially, L_1 and L_2 form segments of the same field line. Segment L_1 lies within a region of constant Φ and hence does not rotate. Segment L_2, however, as part of the outward flux bundle that has passed through D, is rotating at the rate v. L_1 and L_2 therefore become disconnected. This figure is a modified version of Figure 5 from *Priest and Pontin* [2009].

elements that lie below the diffusion region will, at a later time t_1, no longer share the same field line with the plasma elements below the diffusion region. Figure 16 depicts the slippage of field lines. Initially, L_1 and L_2 form segments of the same field line. But because of $\mathbf{E}_{||}$ and the field line rotation, L_1 and L_2 become disconnected. The observational implications are that the spacecraft need not lie in or pass through the nonideal region to detect flows in the fan plane that identify field lines that have engaged with the nonideal region. In fact, field lines that have not done so should have no rotational flow, i.e., $\mathbf{v}_\perp = 0$. (An ideal contribution to $\mathbf{v}_\perp$ is possible but will not be rotationally symmetric.) Moreover, simulations have demonstrated the possibility of spiral type flows about the spine. *Wyper and Jain* [2010] experiment with different types of twist and different vertical (along the spine) bounds on the twist. For same-direction twist above and below the fan plane (consistent with the currents we observe), they find a rotational flow perpendicular to the spine as well as a flow along the spine—forming a spiraling motion around the spine. This is similar to the nonideal magnetohydrodynamic solution found by *Titov and Hornig* [2000] that sustains the spiral null point.

[32] The theoretical prediction of rotational and spiral flow closely resembles the data. The rotational velocity profile is confined to smaller radial distances at larger z'. The radius of rotational flows increases closer to the fan plane. *Pontin et al*. [2004] note that, in the $z' = 0$ (i.e., the fan) plane, both the fan field lines and the plasma outside the diffusion region "rotate like a solid body." This is because the field lines lying in the fan plane have all passed through the diffusion region. The flow we observe, like the prediction, increases for smaller z' and smaller x' and spirals about the spine. Here the observed perpendicular plasma velocity and current structure are consistent with evidence of the torsional spine reconnection predicted by theory. While this type of flow is nonideal, it does not transfer flux across topological boundaries.

[33] Since we have established a local nonideal electric field and a fan current, the question arises as to whether fan reconnection is simultaneously occurring. Since the fan is tilted with respect to the spine, the direction of the fan current along x' is antisymmetric about the y' axis (although at each null point we only have current data on one side of the y' axis). This type of fan current can produce reconnection which, unlike torsional spine reconnection or torsional fan reconnection, transfers flux across the fan plane and thus between topologically distinct regions [*Priest and Pontin*, 2009]. (Torsional fan reconnection is associated with a current that is symmetric about y' and does not tilt the fan. See, for example, *Wyper and Jain* [2010].) While the data are insufficient to establish a stagnation point flow per se, Figure 14 suggests the flow crosses the direction of the fan at an angle. Indeed, the angle between the flow and the fan plane starts at about 20° at larger z' and increases relatively monotonically to about 38° as Cluster gets closer to the null point. However, the fan direction is derived at the position of the centroid, while the flows are derived at the position of Cluster 1, which introduces some uncertainty into the relative local orientations of the fan and the flow. Moreover, though there is a vertical component to the flow and an apparent angle between the flow and the fan plane, the nature of the flow is not quite consistent with the hyperbolic stagnation type flow predicted by *Pontin et al*. [2005a] for fan reconnection. We therefore argue that it is inconclusive whether the nulls are also hosting fan plane reconnection. But theoretical studies to date have examined the effects of spine and fan currents separately and not concurrently. The combination of the two currents might impact the predictions.

4. Summary and Discussion

[34] In this paper, we find in situ evidence for a proposed type of magnetic null point current structure and reconnection that until now has been observed only in the laboratory [*Bogdanov et al*., 1994; *Lukin and Linton*, 2011]. In a moderate to high β region ($\beta \geq 1$) of the magnetosheath, associated by previous authors with filamentary currents, magnetic reconnection, and turbulence [*Retinò et al*., 2007; *Sundkvist et al*., 2007], we find numerous magnetic null points often coupled with current filaments, and often paired or even clustered. In the case of the null pair we consider in this paper, we find oppositely polarized spiral nulls that carry a current and that may be topologically linked. They bear a current along the spine, and a lesser current perpendicular to the spine, and are tilted with respect to their fans. Though the spines of each null are almost parallel to one another, their fans are oriented 25° apart. A superposed epoch analysis based on the linear gradients near the nulls creates a snapshot of each null, removing the motion of the null. The instantaneous field structure of the nulls is consistent with flow of field lines from one null into another. The inversion of the linear relation $\mathbf{B} = \nabla\mathbf{B}\cdot\mathbf{r}$ gives the instantaneous position $\mathbf{r}_0$ of the null, and therefore the null velocity $\mathbf{v}_0$. If the fan surfaces are domed and the fan field lines of each null derive from separate sources, then the fans may intersect along a separator connecting the nulls, even though their spines are almost parallel. Currents may close along looped field lines connecting the nulls. The dominant current along the spine may be part of the current closure, or a larger current sheet in which the nulls are embedded. From the null velocities and a limited set of electric field data, we derive a perpendicular plasma flow in the rest frame of the null that lies outside the diffusion region (where $\mathbf{E}\cdot\mathbf{B} = 0$ is valid). The flows around null A_s are evidence for field lines that pass through a diffusion region centered around the spine current of the null. They spiral in a manner consistent with torsional spine reconnection and may evolve across the fan plane through a concurrent fan reconnection.

[35] These results impact multiple spacecraft analyses of current and magnetic structures in geospace and provide in situ evidence for null point reconnection regimes that are important in the solar corona [*Longcope et al*., 2003; *Parnell*, 2007; *Parnell et al*., 2008; *Parnell et al*., 2010; *Priest and Forbes*, 2000]. In observations, magnetic spatial variations ought to be taken into account when possible. Certainly, the entrainment of nulls indicates 3-D structure. But even in the case of a current "sheet" in the absence of a null point, neglecting a magnetic gradient analysis may obscure an underlying 3-D structure. The 1-D current "sheet" of the spine discovered here actually corresponds to a 3-D topological structure. Furthermore, null point reconnection regimes are important in the solar corona. *Antiochos et al*. [2002] argue, for example, that photospheric line tying limits solar coronal magnetic reconnection to existing null points.

[36] An abundance of magnetic null points observed in the turbulence is significant in two ways. One is that reconnection

may occur at them. But the more important implication is that they represent a topological web of separators that might be reconnecting. If reconnection is indeed occurring at magnetic null points in turbulent regions of the solar wind and the magnetosphere (in particular, in the absence of a strong guide field, such as at the subsolar point), then there may be consequences not only to our interpretation of reconnection in those regions but also to the means of turbulent dissipation. But, more importantly, the presence of clusters of linked nulls, or a web of nulls, is important even where the nulls themselves are not hosting the reconnection. If, instead, most of the reconnection is occurring along the network of separators between the nulls, the network might have a measureable impact on the net reconnection rate. In their study of an MHD model of solar emerging flux, *Parnell et al*. [2010] find that a large rate of flux transfer occurs over a mesh of separators connecting clusters of nulls. *Albright* [1999] relates the density of nulls as a function of the dissipation and integral length scales of a stochastic field and its spectral exponent, and he associates webs of nulls and the null-null lines with current sheet formation and heating. He finds that nulls tend to cluster. The separator linkage between pairs of nulls can also be significant. *Parnell et al*. [2008], for example, determine that reconnection can occur recursively on multiple separators connecting a single pair of nulls, effectively boosting the reconnection rate. Since magnetic null points are observed in the solar wind (in the absence of a guide field) [*Burlaga*, 1967], null point reconnection may be relevant to turbulent dissipation in the solar wind. In their simulation of the 3-D solar wind with the imposition of structures (e.g., flux ropes), waves, and turbulence, *Roberts et al*. [2003] find the development of closed field lines and spiral nulls. If 3-D topology plays a role in increasing the net reconnection rate of the system through many local reconnections, this also has repercussions for reconnection rates as observed by MMS. Dissipation at null point reconnection sites may represent a special case of the more generic scenario of dissipation at current sheets in the case of a guide field.

Appendix A

[37] In this section, we derive the random and systematic errors associated with our analyses and their propagation. First, we derive the sources and propagation of random errors (Table A1). The primary source of random error in B_i is the spin axis offset error, which is the order of tenths of a nT during the dayside season where spacecraft intercalibration is performed (Elizabeth Lucek, former FGM principal investigator (PI), personal communication). Random errors in the magnetic gradients arise from random uncertainties in B_i and the spacecraft positions $\mathbf{r}_{sc}$. We base an order of magnitude estimate for the case of a regular tetrahedron from equation (A1) below, following equation 14.34 derived by *Chanteur* [1998] with $i=m$ and $j=n$, which thus becomes

$$\left(\frac{\partial B_i}{\partial x_j}\right)^2 = \left(\frac{\delta B_i}{2a}\right)^2 + \left(\frac{\delta r_{sc}}{2a}\right)^2 \frac{1}{4a^2}\left[\frac{3}{4}\left(B_{1i}^2 + B_{2i}^2 + B_{3i}^2 + B_{4i}^2\right)\right] \tag{A1}$$

for each gradient component. Here $a \sim 50$ km, ½ the spacecraft separation, δr_{sc} is the uncertainty in spacecraft position, and δB_i is the random uncertainty in B_i (~0.1 nT). Customarily, $\delta r_{sc}/(2a) \sim 0.01$ for Cluster [*Chanteur*, 1998]. Thus, as an approximation to the rms uncertainty in the gradients, we have

$$\left\langle \left(\frac{\partial B_i}{\partial x_j}\right)^2 \right\rangle^{1/2} \cong \left[\left(\frac{0.01}{50}\right)^2 \frac{3}{4} B_{0i}^2 + \left(\frac{0.1}{100}\right)^2\right]^{1/2} = 0.0014 \text{ nT/km}, \tag{A2}$$

where B_{0i} is the average B_i over all four spacecraft and is evaluated the point of peak current (denoted by t_p in the tables). The errors in the current J_i come from errors in the field gradients, and a relative error of less than 10% is typical for a regular tetrahedron [*Robert et al*, 1997], such as we have in this case.

[38] The random uncertainty in the null position and velocity propagates from the uncertainties in the gradients and the magnetic fields. Since $\mathbf{r} - \mathbf{r_0} = \nabla\mathbf{B}^{-1}\mathbf{B}$, the error propagates as

$$\left\langle (\delta \mathbf{r}_0)^2 \right\rangle^{1/2} = \left[\left(\delta\left(\nabla\mathbf{B}^{-1}\right)\mathbf{B}\right)^2 + \left(\nabla\mathbf{B}^{-1}\delta\mathbf{B}\right)^2\right]^{1/2}. \tag{A3}$$

If we assume that the error is the same in each gradient term, then $\delta(\nabla\mathbf{B}^{-1})\mathbf{B} = -\delta(\nabla\mathbf{B})\nabla\mathbf{B}^{-2}\mathbf{B} = -\delta(\nabla\mathbf{B})\ \nabla\mathbf{B}^{-1}(\mathbf{r} - \mathbf{r}_0)$. Thus, for the values evaluated at peak current, $\delta(\nabla\mathbf{B})$ 0.0014 nT/km, and $\delta\mathbf{B}_i$ = 0.1 nT, expression (A3) yields the rms uncertainties for $\mathbf{r}_0$ listed in Table A1. The ensuing rms uncertainties in the null velocity $\mathbf{v}_0$ scale as

$$\left\langle (\delta \mathbf{v}_0)^2 \right\rangle^{1/2} = \left[\left(\frac{d\delta \mathbf{r_0}}{dt}\right)^2 + (\mathbf{v_0}\delta dt)^2\right]^{1/2}, \tag{A4}$$

where δdt is the uncertainty in the time step, which has an average value of 0.067 s. The resulting average value for $\delta\mathbf{v}_0$ for each null is listed in Table A1 in both the spine-aligned and LMN coordinate systems.

[39] The electric field and drift velocity random errors derive from rms uncertainties in E_i and in B_i:

$$\begin{aligned} |\delta v_{d,k}| &= \left|\frac{1}{B^2}\left\{\delta E_i B_j - \delta E_j B_i \right.\right. \\ &\quad \left.\left. + \left[\left(E_i - E_j\right) - \frac{6}{B}\left(E_i B_j - E_j B_i\right)\right]\delta B_i\right\}\right| \Rightarrow \left\langle \left(\delta v_{d,k}\right)^2 \right\rangle^{1/2} \\ &= \left(\left\{\delta E_i B_j\right\}^2 + \left\{E_j B_i\right\}^2 + \left\{\left[\left(E_i - E_j\right)\right.\right.\right. \\ &\quad \left.\left.\left. - \frac{6}{B}\left(E_i B_j - E_j B_i\right)\right]\delta B_i\right\}_i^2 \right)^{1/2}. \end{aligned} \tag{A5}$$

The rms uncertainty in the final null frame plasma flow velocity $\mathbf{v}$ also includes adjustments for the rms error in $\mathbf{v}_0$. The uncertainties δE_i and δE_j include contributions from the error in the spin component of $\mathbf{E}$ and in any misalignment of the spin-plane probe with the actual DC spin-plane field that affects the computation of $\mathbf{E}$ from Cluster 1 (using the assumption that, in a certain time window, the probes line up with the spin plane (DC) field). The former is computed by the instrument data team and provided with the data set. (It will propagate into all three components of $\mathbf{E}$ once the

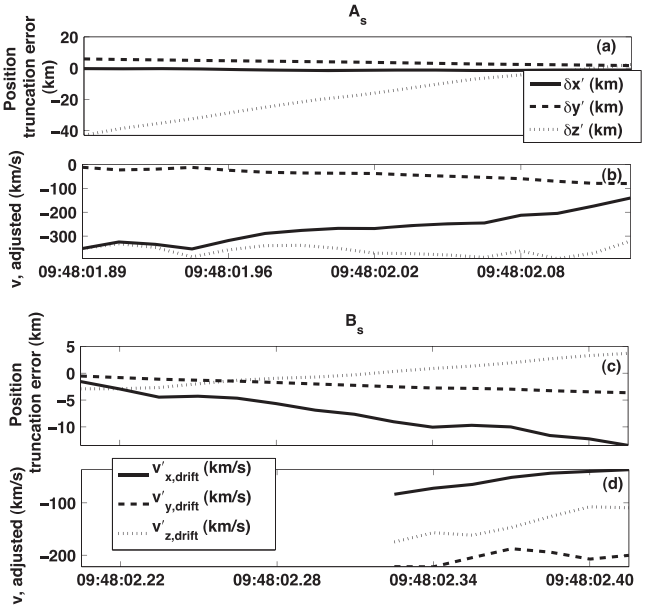

Figure 17. (a) Net systematic error in the three components of the null position. The components are in the spine-aligned coordinate system. (b) Components of the drift flows adjusted for the systematic error in the spine-aligned coordinate system. (c) Corresponding systematic errors in position of null B_s. (d) Adjusted velocity components around null B_s. Though the velocity magnitudes may be affected, the qualitative nature of the flows remains unchanged by adjusting for the systematic errors.

field is rotated out of the spacecraft spin-aligned coordinates.) We estimate the latter by the following argument. We examine the electric fields around null A_s using Cluster 1 data over a time window of 16 time steps dt, where we assume that the probe and he field are approximately aligned. Thus, over $\sim\pm 8dt = \pm 0.12$ s, the spacecraft has spun through $\sim\pm 5.4°$. The corresponding relative error in the spin-plane E_x and E_y is therefore approximately sin(5.4), 10%. (Of course, these

Table A2. Systematic Errors

Quantity	Error at A_s	Error at B_s	Units
$\partial B_i/\partial x_j$ (at t_p) $\sim \nabla\cdot\mathbf{B}/3$	0.005	0.010	nT/km
$B_i \sim 0.002\lvert\mathbf{B}\rvert$	0.0097	0.005	nT
$\mathbf{r}_0$ from truncation	See figure	See figure	km
$<\mathbf{v}'_0>$ from truncation	[0, −20, 182]	[−56, −15, 32]	km/s
$<\mathbf{v}_0>$ from truncation (LMN)	[90, −158, 20]	[56, −33, 14]	km/s

propagate into all components after rotations from the spin coordinate system.) The tally for these contributions produces a random uncertainty in the transformed plasma flow $\mathbf{v}$ as shown in Table A1, where $\mathbf{E}_p = \mathbf{v}_0 \times \mathbf{B}/B^2$.

[40] The dominant contribution to the systematic errors is the truncation in the gradients and the effect this has on the calculation of $\mathbf{r}_0$. There is also a small contribution from a systematic difference of 0.2% between $\mathbf{B}$ measured by FGM by two other instruments (Elizabeth Lucek, personal communication). To estimate the truncation error in the magnetic gradients at any point, we assume that the error is distributed equally across all gradients, such that $\delta(\partial B_i/\partial x_j)_t \sim \nabla\cdot\mathbf{B}/3$, where $\delta(\partial B_i/\partial x_j)_t$ is the truncation error in $(\partial B_i/\partial x_j)$. At the time t_p of peak current at which the gradients are chosen for the position analysis, $\nabla\cdot\mathbf{B}$ is very small. This, along with the systematic uncertainty in $\mathbf{B}$, $\delta\mathbf{B}_s$, leads to a systematic error in null position $\mathbf{r}_0$ of the form

$$\begin{aligned}\delta\mathbf{r}_{0,s} &= -\left(\nabla\mathbf{B}^{-1}\delta\mathbf{B}_s + \delta\left(\nabla\mathbf{B}^{-1}\right)\mathbf{B}\right)\\ &= -\nabla\mathbf{B}^{-1}\left[\delta\mathbf{B}_s - \delta(\nabla\mathbf{B})(\mathbf{r}-\mathbf{r_0})\right]\end{aligned} \tag{A6}$$

with $\delta(\nabla\mathbf{B})_{ij} = \delta(\partial B_i/\partial x_j)$, and where we have used the same mathematical arguments to derive $\delta\mathbf{r}_{0,s}$ as described above in the derivation of the rms uncertainty $<(\delta\mathbf{r}_0)^2>^{1/2}$. The resulting systematic errors are displayed in Figure 17. Table A2 includes the subsequent systematic errors in $\mathbf{v}_0$ averaged over the interval analyzed about each null in both the LMN and the spine-aligned coordinate systems.

Table A1. Random Errors

Quantity	Error at A_s	Error at B_s	Units
B_i, $\lvert\mathbf{B}\rvert$	0.1 nT, 0.3 nT	0.1 nT, 0.3 nT	nT
J_i	0.1	0.1	$\lvert\mathbf{J}\rvert$
$\partial B_i/\partial x_j$, from B_i, $\mathbf{r}_{sc}$	0.0014	0.0014	nT/km
$\mathbf{r}'_0$, from B_i, $\partial B_i/\partial x_j$	[4.63, 2.32, 13.03]	[10.19, 2.31, 4.79]	km
$\mathbf{r}_0$, from B_i, $\partial B_i/\partial x_j$ (LMN)			
Time step dt	0.067	0.067	dt
$\mathbf{v}'_0$ from B_i, $\partial B_i/\partial x_j$, dt	[32.38, 11.30, 70.80]	[9.26, 5.78, 8.67]	km/s
$\mathbf{v}_0$ from B_i, $\partial B_i/\partial x_j$, dt (LMN)	[12.95, 77.02, 11.08]	[9.18, 8.71, 5.83]	km/s
E_i, from spin axis (LMN)	[0.36, −0.31, −0.14]	[0.06, −0.05, −0.02]	mV/m
E_i, from single-probe pair alignment, $\sim\pm 0.1$ E_i (A_s only) (LMN)	[0.04, −0.03, 0.18]		mV/m
E_i from single-probe pair alignment and spin axis combined (A_s only) (LMN)	[0.39, −0.34, 0.04]		mV/m
$\mathbf{v}'_d = \mathbf{E}'\times\mathbf{B}'/\lvert\mathbf{B}\rvert^2$	[5.41, 24.99, 21.30]	[3.75, 9.57, 33.65]	km/s
$\mathbf{v}_d = \mathbf{E}\times\mathbf{B}/\lvert\mathbf{B}\rvert^2$ (LMN)	[5.73, 20.66, 25.48]	[4.22, 33.30,12.85]	km/s
$\mathbf{v}' = (\mathbf{E}'+\mathbf{E}'_p)\times\mathbf{B}'/\lvert\mathbf{B}'\rvert^2$ in null rest frame	[33.0, 27.5, 74.0]	[10.7, 13.4, 34.7]	km/s
$\mathbf{v} = (\mathbf{E}+\mathbf{E}_p)\times\mathbf{B}/\lvert\mathbf{B}\rvert^2$ in null rest frame (LMN)	[14.2, 80.0, 28.0]	[10.9, 34.3, 14.2]	km/s
$\mathbf{v}'$ average relative error ($\delta v_i/<v_i>$) in null rest frame	[0.16, 0.60, 0.20]	[0.08, 0.11, 0.09]	

[41] **Acknowledgments.** The authors wish to thank Melvyn L. Goldstein, Mats André, and Adolfo F. Viñas for helpful discussions. D. E. Wendel wishes to acknowledge the assistance of Kyoung-Joo Hwang for verification of the MVA. We wish to acknowledge data provided by the Cluster Active Archive and thank the FGM PI Elizabeth Lucek and the EFW PI Mats André and their teams for making the data available. This research was supported by NASA funding for the Cluster mission and for the MMS Interdisciplinary Science grant to the Goddard Space Flight Center.

References

Albright, B. J. (1999), The density and clustering of magnetic nulls in stochastic magnetic fields, *Phys. Plasmas*, *6*(11), 4222–4228, doi:10.1063/1.873689.

Antiochos, S. K., J. T. Karpen, and C. R. DeVore (2002), Coronal magnetic field relaxation by null-point reconnection, *Astrophys. J.*, *575*(1), 578–584, doi:10.1086/341193.

Beveridge, C., E. R. Priest, and D. S. Brown (2002), Magnetic topologies due to two bipolar regions, *Sol. Phys.*, *209*(2), 333–347.

Bhattacharjee, A., Y. M. Huang, H. Yang, and B. Rogers (2009), Fast reconnection in high-Lundquist-number plasmas due to the plasmoid Instability, *Phys. Plasmas*, *16*(11), 112101–112102-5, doi:10.1063/1.3264103.

Bogdanov, S. Y., V. B. Burilina, V. S. Markov, and A. G. Frank (1994), Formation of current sheets in 3D magnetic-felds with a null point, *JETP Lett.*, *59*(8), 537–541.

Boldyrev, S. (2006), Spectrum of magnetohydrodynamic turbulence, *Phys. Rev. Lett.*, *96*(11), 115001, doi:10.1103/PhysRevLett.96.115002.

Burlaga, L. F. (1967), *Micro-scale structures in the interplanetary medium*, NASA technical report, NASA Goddard Space Flight Center, Greenbelt, MD, 1–26.

Chanteur G. (1998), Spatial interpolation for four spacecraft: Theory, in *Analysis Methods for Multi-Spacecraft Data*, edited by G. Paschmann, and P. W. Daley, pp. 349–369, ESA Publications Division, Noordwijk.

Che, H., J. F. Drake, and M. Swisdak (2011), A current filamentation mechanism for breaking magnetic field lines during reconnection, *Nature*, *474*(7350), 184–187, doi:10.1038/nature10091.

Coleman P. J. (1968), Turbulence and dissipation in solar-wind plasma, *Eos Trans. AGU*, *49*(1), 263.

Cowley, S. C., D. W. Longcope, and R. N. Sudan (1997), Current sheets in MHD turbulence, *Phys. Rep.*, *283*, 227–251, doi:10.1016/S0370-1573(96)00064-6.

Cranmer, S. R., W. H. Matthaeus, B. A. Breech, and J. C. Kasper (2009), Empirical constraints on proton and electron heating in the fast solar wind, *Astrophys. J.*, *702*(2), 1604–1614, doi:10.1088/0004-637X/702/2/1604.

Daughton, W., V. Roytershteyn, H. Karimabadi, L. Yin, B. J. Albright, B. Bergen, and K. J. Bowers (2011), Role of electron physics in the development of turbulent magnetic reconnection in collisionless plasmas, *Nat. Phys.*, *7*(7), 539–542, doi:10.1038/nphys1965.

Deng, X. H. et al. (2009), Dynamics and waves near multiple magnetic null points in reconnection diffusion region, *J. Geophys. Res.*, *114*, A07216, doi:10.1029/2008JA013197.

Dorelli, J. C., A. Bhattacharjee, and J. Raeder (2007), Separator reconnection at Earth's dayside magnetospause under generic northward interplanetary magnetic field conditions, *J. Geophys. Res.*, *112*, A002202, doi:10.1029/2006JA011877.

Dunlop, M. W., A. Balogh, K.-H. Glassmeier, and P. Robert (2002), Four-point Cluster application of magnetic field analysis tools: the curlometer, *J. Geophys. Res.*, *107*(A11), 1385, doi:10.1029/2001JA005089.

Eastwood, J. P., T. D. Phan, S. D. Bale, and A. Tjulin (2009), Observations of turbulence generated by magnetic reconnection, *Phys. Rev. Lett.*, *102*(3), 035001, doi:10.1103/PhysRevLett.102.035001.

Galsgaard, K., and D. I. Pontin (2011a), Steady state reconnection at a single 3D magnetic null point, *Astron. Astrophys.*, *529*(A20), doi:10.1051/0004-6361/201014359.

Galsgaard, K., and D. I. Pontin (2011b), Current accumulation at an asymmetric 3D null point caused by generic shearing motions, *Astron. Astrophys.*, *534*(A2), doi:10.1051/0004-6361/201117532.

Goldstein, M. L., D. A. Roberts, and W. H. Matthaeus (1995), Magnetohydrodynamic turbulence in the solar-wind, *Annu. Rev. Astron. Astrophys.*, *33*, 283–325, doi:10.1146/annurev.aa.33.090195.001435.

Greco, A., S. Servidio, W. H. Matthaeus, and P. Dmitruk (2010), Intermittent structures and magnetic discontinuities on small scales in MHD simulations and solar wind, *Planet. Space Sci.*, *58*(14-15), 1895–1899, doi:10.1016/j.pss.2010.08.019.

Greco A., W. H. Matthaeus, S. Servidio, P. Chuychai, and P. Dmitruk (2009), Statistical analysis of discontinuities in solar wind ACE data and comparison with intermittent MHD turbulence, *Astrophys. J. Lett.*, *691*(2), L111-L114, doi:10.1088/0004-637X/691/2/L111.

Greene, J. M. (1992), Locating 3-dimensional roots by a bisection method, *J. Comput. Phys.*, *98*(2), 194–198, doi:10.1016/0021-9991(92)90137-N.

Harvey C. C. (1998), Spatial gradients and the volumetric tensor, in *Analysis Methods for Multi-Spacecraft Data*, edited by G. Paschmann, and P. W. Daley, pp. 307–322, ESA Publications Division, Noordwijk.

Haynes, A. L., and C. E. Parnell (2007), A trilinear method for finding null points in a three-dimensional vector space, *Phys. Plasmas*, *14*(8), 082107-082107-8, doi:10.1063/1.2756751.

He, J. S., et al. (2008), Electron trapping around a magnetic null, *Geophys. Res. Lett.*, *35*(14), L14104, doi:10.1029/2008GL034085.

Ji, H. T., S. Terry, M. Yamada, R. Kulsrud, A. Kuritsyn, and Y. Ren (2004), Electromagnetic fluctuations during fast reconnection in a laboratory plasma, *Phys. Rev. Lett.*, *92*(11), 115001, doi:10.1103/PhysRevLett.92.115001.

Lau, Y. T., and J. M. Finn (1990), 3-Dimensional kinematic reconnection in the presence of field nulls and closed field lines, *Astrophys. J.*, *350*(2), 672–691, doi:10.1086/168419.

Lazarian, A., A. Beresnyak, H. Yan, M. Opher, and Y. Liu (2009), Properties and selected implications of magnetic turbulence for interstellar medium, local bubble and solar wind, *Space Sci. Rev.*, *143*(1-4), 387–413, doi:10.1007/s11214-008-9452-y.

Longcope, D. W., D. S. Brown, and E. R. Priest (2003), On the distribution of magnetic null points above the solar photosphere, *Phys. Plasmas*, *10*(8), 3321–3334, doi:10.1063/1.1590983.

Lukin, V. S., and M. G. Linton (2011), Three-dimensional magnetic reconnection through a moving magnetic null, *Nonlinear Processes Geophys.*, *18*(6), 871–882, doi:10.5194/npg-18-871-2011.

Matthaeus, W. H., and S. L. Lamkin (1985), Rapid magnetic reconnection caused by finite-amplitude fluctuations, *Phys. Fluids*, *28*(1), 303–307, doi:10.1063/1.865147.

Matthaeus, W. H., and S. L. Lamkin (1986), Turbulent magnetic reconnection, *Phys. Fluids*, *29*(8), 2513–2534, doi:10.1063/1.866004.

Matthaeus, W. H., S. Oughton, D. H. Pontius, and Y. Zhou (1994), Evolution of energy-containing turbulent eddies in the solar-wind, *J. Geophys. Res.*, *99*(A10), 19267–19287, doi:10.1029/94JA01233.

Matthaeus W. H., P. Dmitruk, S. Oughton, and D. Mullan (2003), Turbulent dissipation in the solar wind and corona, AIP Conf. Proc., *679*, 427–432, doi:10.1063/1.1618627.

Osman, K. T., and T. S. Horbury (2009), Multi-spacecraft measurement of anisotropic power levels and scaling in solar wind turbulence, *Ann. Geophys.*, *27*(8), 3019–3025, doi:10.5194/angeo-27-3019-2009.

Osman, K. T., W. H. Matthaeus, A. Greco, and S. Servidio (2011), Evidence for inhomogeneous heating in the solar wind, *Astrophys. J. Lett.*, *727*(1), L11, doi:10.1088/2041-8205/727/1/L11.

Parnell, C. E. (2007), Multiply connected source and null pairs, *Sol. Phys.*, *242*(1-2), 21–41, doi:10.1007/s11207-007-0329-0.

Parnell, C. E., A. L. Haynes, and K. Galsgaard (2008), Recursive reconnection and magnetic skeletons, *Astrophys. J.*, *675*(2), 1656–1665, doi:10.1086/527532.

Parnell C. E., R. C. Maclean, and A. L. Haynes (2010), The detection of numerous magnetic separators in a three-dimensional magnetohydrodynamic model of solar emerging flux, *Astrophys. J. Lett.*, *725*(2), L214–L218, doi:10.1088/2041-8205/725/2/L214.

Parnell, C. E., J. M. Smith, T. Neukirch, and E. R. Priest (1996), The structure of three-dimensional magnetic neutral points, *Phys. Plasmas*, *3*(3), 759–770, doi:10.1063/1.871810.

Parnell, C. E., T. Neukirch, J. M. Smith, and E. R. Priest (1997), Structure and collapse of three-dimensional magnetic neutral points, *Geophys. Astrophys. Fluid Dyn.*, *84*(3-4), 245–271, doi:10.1080/03091929708208979.

Pontin, D. I. (2011), Three-dimensional magnetic reconnection regimes: A review, *Adv. Space Res.*, *47*(9), 1508–1522, doi:10.1016/j.asr.2010.12.022.

Pontin, D. I., and K. Galsgaard (2007), Current amplification and magnetic reconnection at a three-dimensional null point: Physical characteristics, *J. Geophys. Res.*, *112*(A3), A03103, doi:10.1029/2006JA011848.

Pontin, D. I., G. Hornig, and E. R. Priest (2004), Kinematic reconnection at a magnetic null point: Spine-aligned current, *Geophys. Astrophys. Fluid Dyn.*, *98*(5), 407–428, doi:10.1080/0309192042000272324.

Pontin, D. I., G. Hornig, and E. R. Priest (2005a), Kinematic reconnection at a magnetic null point: Fan-aligned current, *Geophys. Astrophys. Fluid Dyn.*, *99*(1), 77–93, doi:10.1080/03091920512331328071.

Pontin, D. I., A. Bhattacharjee, and K. Galsgaard (2007), Current sheet formation and nonideal behavior at three-dimensional magnetic null points, *Phys. Plasmas*, *14*(5), 052106-052106-13, doi:10.1063/11.2722300.

Pontin, D. I., A. K. Al-Hachami, and K. Galsgaard (2011), Generalised models for torsional spine and fan magnetic reconnection, *Astron. Astrophys.*, *533*(A78), doi:10.1051/0004-6361/201117250.

Pontin, D. I., K. Galsgaard, G. Hornig, and E. R. Priest (2005b), A fully magnetohydrodynamic simulation of three-dimensional non-null

reconnection, *Phys. Plasmas*, *12*(5), 052307-052307-10, doi:10.1063/1.1891005.

Priest, E. R., and V. S. Titov (1996), Magnetic reconnection at three-dimensional null points, *Philos. Trans. R. Soc. A*, *354*(1721), 2951–2992, doi:10.1098/rsta.1996.0136.

Priest, E. R., and T. Forbes (2000), *Magnetic Reconnection: MHD Theory and Applications*, Cambridge University Press, Cambridge, UK, pp. 600.

Priest, E. R., and D. I. Pontin (2009), Three-dimensional null point reconnection regimes, *Phys. Plasmas*, *16*(12), 122101-122101-15, doi:10.1063/1.3257901.

Retinò, A., D. Sundkvist, A. Vaivads, F. Mozer, M. Andre, and C. J. Owen (2007), In situ evidence of magnetic reconnection in turbulent plasma, *Nat. Phys.*, *3*(4), 235–238, doi:10.1038/nphys574.

Robert P., M. W. Dunlop, A. Roux, and G. Chanteur (1998), Accuracy of current density determination, in *Analysis Methods for Multi-Spacecraft Data*, edited by G. Paschmann, and P. W. Daley, pp. 395–418, ESA - Publications Division, Noordwijk.

Roberts, D. A., M. L. Goldstein, and A. Deane (2003), Three-dimensional MHD simulation of solar wind structure, *AIP Conf. Proc.*, *679*, 133–136, doi:10.1063/1.1618559.

Sahraoui, F., M. L. Goldstein, P. Robert, and Y. V. Khotyaintsev (2009), Evidence of a cascade and dissipation of solar-wind turbulence at the electron gyroscale, *Phys. Rev. Lett.*, *102*(23), 231102, doi:10.1103/PhysRevLett.102.231102.

Sahraoui, F., M. L. Goldstein, G. Belmont, P. Canu, and L. Rezeau (2010), Three dimensional anisotropic k-spectra of turbulence at subproton scales in the solar wind, *Phys. Rev. Lett.*, *105*(13), 131101, doi:10.1103/PhysRevLett.105.131101.

Schrijver, C. J., and A. M. Title (2002), The topology of a mixed-polarity potential field, and inferences for the heating of the quiet solar corona, *Sol. Phys.*, *207*(2), 223–240.

Servidio, S., W. H. Matthaeus, M. A. Shay, P. A. Cassak, and P. Dmitruk (2009), Magnetic reconnection in two-dimensional magnetohydrodynamic turbulence, *Phys. Rev. Lett.*, *102*(11), 115003, doi:10.1103/PhysRevLett.102.115003.

Servidio, S., W. H. Matthaeus, M. A. Shay, P. Dmitruk, P. A. Cassak, and M. Wan (2010), Statistics of magnetic reconnection in two-dimensional magnetohydrodynamic turbulence, *Phys. Plasmas*, *17*(3), 032315-032315-17, doi:10.1063/1.3368798.

Shi, Q. Q., C. Shen, M. W. Dunlop, Z. Y. Pu, Q. G. Zong, Z. X. Liu, E.3Lucek, and A. Balogh (2006), Motion of observed structures calculated from multi-point magnetic field measurements: Application to Cluster, *Geophys. Res. Lett.*, *33*(8), L08109, doi:10.1029/2005GL025073.

Smith, D., S. Ghosh, P. Dmitruk, and W. H. Matthaeus (2004), Hall and turbulence effects on magnetic reconnection, *Geophys. Res. Lett.*, *31*(2), L02805, doi:10.1029/2003GL018689.

Sonnerup, B. U. Ö., and M. Scheible (1998), Minimum and maximum variance analysis, in *Analysis Methods for Multi-Spacecraft Data*, edited by G. Paschmann, and P. W. Daley, pp. 185–220, ESA - Publications Division, Noordwijk.

Strauss, H. R. (1988), Turbulent reconnection, *Astrophys. J.*, *326*, 412–417.

Sundkvist, D., A. Retinò, A. Vaivads, and S. D. Bale (2007), Dissipation in turbulent plasma due to reconnection in thin current sheets, *Phys. Rev. Lett.*, *99*(2), 025004, doi:10.1103/PhysRevLett.99.025004.

Titov, V. S., and G. Hornig (2000), Magnetohydrodynamic flows sustaining stationary magnetic nulls, *Phys. Plasmas*, *7*(9), 3542–3550, doi:10.1063/1.1286862.

Vasquez, B. J., C. W. Smith, K. Hamilton, B. T. MacBride, and R. J. Leamon (2007), Evaluation of the turbulent energy cascade rates from the upper inertial range in the solar wind at 1 AU, *J. Geophys. Res.*, *112*(A7), A07101, doi:10.1029/2007JA012305.

Verma, M. K., D. A. Roberts, and M. L. Goldstein (1995), Turbulent heating and temperature evolution in the solar-wind plasma, *J. Geophys. Res.*, *100*(A10), 19839–19850, doi:10.1029/95JA01216.

Wan, M., W. H. Matthaeus, H. Karimabadi, V. Roytershteyn, M. Shay, P. Wu, W. Daughton, B. Loring, and S. C. Chapman (2012), Intermittent dissipation at kinetic scales in collisionless plasma turbulence, *Phys. Rev. Lett.*, *109*(19), 195001, doi:10.1103/PhysRevLett.109.195001.

Wendel, D. E., and P. H. Reiff (2009), Magnetopause reconnection impact parameters from multiple spacecraft magnetic field measurements, *Geophys. Res. Lett.*, *36*, L20108, doi:10.1029/2009GL040228.

Wyper, P., and R. Jain (2010), Torsional magnetic reconnection at three-dimensional null points: A phenomenological study, *Phys. Plasmas*, *17*(11), 092902-092902-10, doi:10.1063/1.3480639.

Xiao, C. J. et al. (2006), In situ evidence for the structure of the magnetic null in a 3D reconnection event in the Earth's magnetotail, *Nat. Phys.*, *2*(7), 478–483, doi:10.1038/nphys342.

Zank G. P., W. H. Matthaeus, and C. W. Smith (1996), Evolution of turbulent magnetic fluctuation power with heliocentric distance, in *Solar Wind Eight*: *Proceedings of the Eighth International Solar Wind Conference*, *382*, 630–633, doi:10.1063/1.51449.